View metadata, citation and similar papers at core.ac.uk

brought to you by CORE

provided by Warwick Research Archives Portal Repository

Manuscript version: Author's Accepted Manuscript
The version presented in WRAP is the author's accepted manuscript and may differ from the published version or Version of Record.

Persistent WRAP URL:
http://wrap.warwick.ac.uk/115518

How to cite:
Please refer to published version for the most recent bibliographic citation information. If a published version is known of, the repository item page linked to above, will contain details on accessing it.

Copyright and reuse:
The Warwick Research Archive Portal (WRAP) makes this work by researchers of the University of Warwick available open access under the following conditions.

Copyright © and all moral rights to the version of the paper presented here belong to the individual author(s) and/or other copyright owners. To the extent reasonable and practicable the material made available in WRAP has been checked for eligibility before being made available.

Copies of full items can be used for personal research or study, educational, or not-for-profit purposes without prior permission or charge. Provided that the authors, title and full bibliographic details are credited, a hyperlink and/or URL is given for the original metadata page and the content is not changed in any way.

Publisher's statement:
Please refer to the repository item page, publisher's statement section, for further information.

For more information, please contact the WRAP Team at: wrap@warwick.ac.uk.

warwick.ac.uk/lib-publications

Nanoscale Electrochemical Mapping

Cameron L. Bentley,[1] James Edmondson,[1,2] Gabriel N. Meloni,[1] David Perry,[1] Viacheslav Shkirskiy,[1] Patrick R. Unwin[1,*]

[1]Department of Chemistry, [2]MAS Centre for Doctoral Training, University of Warwick, Coventry, CV4 7AL, United Kingdom

*Corresponding author:

p.r.unwin@warwick.ac.uk

1. Introduction

Surfaces and interfaces, of both practical and fundamental interest, have long been recognized to be complex, yet while there are many microscopy and spectroscopy methods for imaging structure, topography and surface chemical composition at high spatial resolution, there are relatively few techniques for mapping associated chemical fluxes in the near-interface region. In this regard, scanning electrochemical probe microscopy (SEPM), which utilizes a small scale electrode probe as an imaging device, has had a unique place in the scanning probe microscopy (SPM) family of techniques, in being able to map chemical fluxes and interfacial reactivity. For a long time, techniques such as scanning electrochemical microscopy (SECM) were largely stuck at the micron – or larger – scale in terms of spatial resolution, but recent years have seen spectacular progress, such that a variety of different types of SEPM technique are now available and 10s of nm spatial resolution is becoming increasingly accessible. This step-change in capability is opening many new opportunities for the characterization of flux processes and interfacial activity in a whole raft of systems, including electrode surfaces, electromaterials, soft matter, living cells and tissues.

Most of the significant developments in nanoscale SEPM have occurred since 2010 and a previous review in this series captured major advances in scanning ion conductance microscopy (SICM), SECM, scanning electrochemical cell microscopy (SECCM) and hybrids of these techniques primarily in the period 2014-16.[1] We also produced a review article in 2016 that described new frontiers that are being opened up from advances in nanoscale electrochemical imaging.[2] Mainly covering the past 3 years, the present article highlights advances in each of the main SEPM techniques, and various hybrid SEPM methods. We also cover electrochemical - scanning tunneling microscopy (EC-STM), where there have been interesting developments in high-resolution electrochemical mapping and in determining changes in electrode structure in electrochemical processes, which has been the main traditional use of EC-STM. We note in passing that there has been considerable progress in single molecule conductance and electrochemistry studies with EC-STM, as highlighted in recent reviews,[3,4] but this field is beyond the scope of this article.

In selecting material for inclusion in this article, we have used the common definition of nanoscale as being 100 nm or smaller, and conveniently use the tip radius as the measure. We note that there is a wealth of literature concerning SECM that uses micron or larger scale probes and so much of this work is not covered. However, there are some example applications

of SECM with sub-micron scale resolution that will be of interest to the nanoscale community and so we reference these as appropriate. SICM and SECCM easily attain the nanoscale definition, due to the ease of fabrication and use of nanopipet probes, and the fact that these techniques incorporate and measure substrate topography, as well as other functional properties. We have recently reviewed aspects of both techniques over the past 2 years.[5,6] Some other SEPM-related methods have remained at the 10s of micron scale and we briefly mention these later as areas where there is room for innovation.

Alongside developments in SEPMs, various optical methods are increasingly finding application for visualizing electrode activity, and during the period covered by the review there are initial signs of the combination of SEPMs and optical techniques. We thus very briefly mention some of these methods, noting that there have been recent reviews that include electrochemical applications of super-resolution microscopy, plasmonic-based imaging techniques and holography.[7,8]

With the translation of SEPM to the nanoscale, the preparation and understanding of the behavior of nanoelectrodes and nanopipets is imperative, for which there are recent scholarly reviews.[9,10] We also point the interested reader to relevant reviews from the period that cover SECM characterization of electrocatalysts, [11] a very recent review on the application of SEPM in general to electrocatalysis,[12] microelectrochemical studies of corrosion,[13] and high-resolution investigations of energy storage materials.[14,15] The most comprehensive review of SECM ever written, which serves as a practical guide to the new entrant and experienced researcher alike, was also published in the period.[16] The popularity of SECM, in particular, and SEPM in general, for single cell electrochemical imaging and life sciences applications, is reflected in a number of recent review articles.[17-22]

SEPM is a key enabling technology for the emerging fields of single entity electrochemistry and electrochemistry at nano-interfaces, for which there were seminal *Faraday Discussion* meetings in 2016 and 2018, respectively. The published volumes of these meetings[23,24] contain not only original papers, but also extensive discussions of key issues. A very recent perspective of single entity electrochemistry places SEPM techniques alongside broader developments in this exciting field,[25] some of which we discuss herein.

2. Scanning Electrochemical Microscopy (SECM)

2.1 Overview of Operational Principles

SECM is the best-known technique in the SEPM family and has been widely adopted since its inception in the late 1980s.[26,27] The operational principles of SECM and its applications have been covered in a number of recent reviews.[16,28-30] Using small-scale electrodes (originally micron-scale ultramicroelectrodes, UMEs, and most recently nanoelectrodes, Section 2.2) as a scanning probe tip, SECM is capable of resolving either the topography or (electro)chemical activity (albeit not usually simultaneously) of substrates immersed in a solution (electrolyte) bath. This is achieved by monitoring the electrochemical response of the scanning tip when it is brought into close proximity with a substrate surface (*e.g.*, Figure 1A-i). In essence, the extent and nature of the perturbations caused by the substrate on the recorded signal at the SECM tip is used to infer on the substrate properties.[31,32] For instance, considering the most simple amperometric tip, an insulating substrate hinders the diffusion of an electroactive solute towards the tip, resulting in a diminished current (*i.e.*, negative feedback),[26,31] while a conducting substrate poised at the appropriate potential (externally biased or unbiased) may regenerate the active species, enhancing the tip current by creating a positive feedback loop, or redox shuttling between the tip and surface (as in Figure 1A-i).

While involving UMEs on the hundreds of nm to micron-scale and not mapping, it is worth mentioning that recent work has sought to decrease the gap size in dual-electrode SECM, where a tip electrode is positioned close to a substrate electrode, to create a device with high tip-substrate diffusion rates of soluble redox couples, thereby extending the upper kinetic limit accessible for the measurement of fast electron-transfer kinetics[33] and the detection of short-lifetime transient species.[34,35] A small gap size, however, requires careful analysis and modeling of ion migration[36,37] and double layer effects at the electrodes[33,36,38] and the glass or quartz sheath[38] that surrounds the active part of the tip. Thus, recent treatments of mass-transport in SECM have considered solutions to the Nernst-Planck equation and Poisson equation with charged interfaces.[38] Such considerations extend to nanoscale SECM probes used for imaging, which are usually deployed close to the substrate (within a distance of a tip radius or so).

As the first SEPM, SECM continues to be widely used,[39,40] and is applicable to a range of chemical and electrochemical systems.[1,16,17,28,29,41,42] There have been recent interesting methodological developments such as the use of a line electrode probe to speed up image

acquisition rates.[43] However, as conventional SECM lacks independent positional feedback of the tip and relies on constant height scanning,[16,44] there are naturally practical limitations when attempting to investigate (electro)chemical systems at the single entity level, *e.g.*, single nanoparticles (NPs) or particular sites on a complex surface such as step edges, defined crystallographic facets or grain boundaries (GBs), for which nanoscale electrochemical flux mapping is proving to be particularly powerful.[45,46] Significant efforts have being made in the past half-decade to use multifunctional probes and combined techniques,[2,47] as described later in this article. Here, we consider recent efforts towards nanoscale reaction mapping by translating conventional SECM methods and instrumentation.

2.2 Approaching the Nanoscale with SECM

A recent review has discussed the translation of SECM to the nanoscale.[40,44] Considerations for nanoscale SECM probe tips include ease of fabrication, lifetime, reproducibility and electrochemical behavior over the long periods of a scan, and technical issues around positioning and scanning within a distance of a tip radius or so from a surface (*i.e.*, 10s of nm), in a constant height mode, without independent distance control or positional feedback. To address this issue, a few innovative approaches are worth mentioning, such as the use of a hopping scan protocol, where the scanning (nanoelectrode) tip performs an approach curve from bulk solution towards the substrate at every image pixel of an electrochemical map. By comparing the current recorded at bulk with the one near the surface, the electrode can be stopped consistently at a desired current variation (*i.e.*, feedback set-point, albeit that the substrate activity must be known *a-priori*). This approach effectively eliminates instrumental drift, such as thermal drift of the piezoelectric actuators commonly used for tip positioning,[48] allowing the tip to be precisely positioned near the substrate and, due to the retract distance adopted during the hopping procedure, used to scan substrates with pronounced topographical features.[49]

Another recent approach to solve the problem of precisely approaching a tip close to a substrate surface involves partially modifying the interface (*e.g.*, with a flexible polymer spot) to make it "soft".[50] This "soft" interface allows the tip to be approached very close to (and even into contact with) the surface, without sustaining significant damage (*i.e.*, change in tip geometry and/or electrochemical response). The "soft" nature of the substrate also allowed for fast tip approaches to be performed, at speeds up to 100-fold the ones normally employed in SECM with nanometric tips, which can result in a significant decrease in scanning times. Once

approached to the "soft spot" at the substrate, the tip can be laterally translated to a "hard" area of the substrate, allowing this approach to be employed with a range of different materials.[50]

Interestingly, this latter approach to positioning electrodes also has significant implications for the characterization of nanoelectrodes. At the nanoscale, SECM probes are often, but not exclusively,[51] solid electrodes that consist of a conductive material (commonly noble metals or carbon) encapsulated within an inert insulating material (*e.g.*, glass or quartz) outer sheath.[52,53] While the dimensions of conventional (micron to 10s of micron scale electrode) SECM probes are readily determined (*e.g.*, the size of the metal wire used is known, visual inspection is easily made by optical microscopy, and steady-state voltammetry reveals the electrode size and dimensions[54]), such easy methods obviously do not translate to the nanoscale. In particular, voltammetric measurements alone may provide misleading information regarding the true electrode size and geometry,[55,56] because an idealized geometry has to be assumed and small imperfections can have a significant effect on nanoscale mass-transport and the associated voltammetry. Approach curves towards soft substrates, mentioned above, also provide critical information regarding the tip geometry without the risk of destroying the tip.[50] Nonetheless, non-ideal tip geometry and tip-substrate misalignment can still significantly impact the electrochemical response in SECM approach curves, and thus the careful use of electron microscopy (notably transmission electron microscopy, TEM) to allow the proper characterization of small-scale SECM probes is increasingly advocated.[57] Accurate knowledge of tip geometry is essential for quantitative analysis of experimental data with simulation models.[38,58-61]

2.3 Fabrication of Nanometer-sized SECM tips

There are a number of reports on the fabrication of metal electrodes on the sub-100 nm scale.[42,62,63] Due to the large impact of electrode geometry on the electrochemical response, further fabrication steps are often used to shape the electrode and thus tailor its electrochemical response.[64-66] On this note, focused ion beam (FIB) milling can be an important step, used to sculpt a tip to the desired geometry,[66,67] as in the tip shown in Figure 1A-ii,[65] although this obviously extends the complexity and cost of tip manufacture. Such tips have been used to image nanomaterials, as summarized in Figure 1B, which we discuss in more detail below. Recent efforts have demonstrated that the fabrication of nm-sized electrodes, with geometries suitable for SECM experiments, can be achieved using less expensive and time-consuming methods and materials. By replacing laser-heated micropipet pullers by more affordable ones

with resistive coil-based heating and thus using glass capillary tubes (instead of quartz), Pt nanoelectrodes were fabricated and successfully employed for high-resolution imaging of metallic substrates (Pt and Ti nano-bands and single AuNPs anchored to a thiol-covered Au substrate) and the catalytic activity of lactate-oxidase modified Au substrates.[49,68] It should also be noted that some laboratories have reported that nm-sized metal electrodes can be easily damaged without severe precautions,[44,69] which adds to the costs and time demands involved in the fabrication and handling of SECM tips.

An ingenious alternative for making SECM tips is based on the pyrolysis of a carbon source (usually butane gas) under an Ar atmosphere to produce carbon inside freshly pulled quartz nanopipets,[55,70] as originally introduced by Takahashi *et al*.[68] and developed by others.[53] This is a relatively fast method, but as it is a manual procedure, the creation of a tip electrode that is flush with the end of the surrounding quartz sheath is something of an art, with recessed (inside of the pipet bore), overfilled or damaged electrodes being commonplace. An advantage of these probes is that the carbon filling is readily visualized with TEM and FIB can be used to square off a recessed electrode,[42,71] as with metal nanoelectrodes, discussed above. A more sophisticated approach to the carbon pyrolysis fabrication method was recently reported, based on the use of an automated robotic system (Figure 2A-i and ii), resulting in a higher success rate, reproducibility and quality of nm-sized carbon tips.[57] By removing the inherent inaccuracies of the manual operation procedures used previously, the influences of multiple pyrolysis parameters on the final SECM tip geometry were elucidated, leading to a more robust and reproducible fabrication protocol (Figure 2B).

Recent reports have explored the use of different solution compositions inside the nanopipet and in the bulk solution in which the tip is placed to drive the formation of metallic NPs in the pipet bore where the two solutions contact. The resulting structures can behave as bipolar electrodes, and metal electrodeposition can be precisely controlled and monitored by applying a driving potential between a quasi-reference counter electrode (QRCE) located inside the pipet and one in bulk solution, yielding nanometer-sized metal electrodes (Figure 2C). This approach can reportedly produce electrodes quickly and reproducibly, with radii on the 10s of nm scale, and robust electrochemical responses,[72-75] ideally suited to mapping electrochemical substrate properties with nanoscale resolution.[74] Pt has also been grown at the end of a nanopipet and at nanopores using FIB to make bipolar nanoscale electrodes and such an approach may be valuable in the future for making SECM tips.[76,77]

SECM with tips on the sub-micron to 100s of nm scale have been deployed for electrochemical mapping of a wide spectrum of processes, ranging from studies of the corrosion of steel,[78] electrochemical characterization of complex electrocatalytic materials,[79] assessment of basal surface and step-edge redox activity in MoS_2 devices,[80] ion intercalation into graphene,[81] and investigation of charge storage capacity on redox active colloids.[82] The latter study is particularly noteworthy as it involved the use of SECM on a Raman microscopy platform. The combination of SECM and other SEPMs with co-located microscopy or micro-spectroscopy is a developing trend that is proving powerful for providing holistic views of structure-function at high spatial resolution. Beyond the investigation of electrodes and electroactive materials, SECM with nanoscale probes continues to be popular in life sciences applications, for example, investigating molecular uptake at the single cell level.[61]

Recent works have also showcased SECM measurements on the 10s of nm scale, such as the investigation of the homogeneity and passivity of thiophenol diazonium films graphitized over highly ordered pyrolytic graphite (HOPG) substrates.[83] The properties of the surface heterogeneities (*e.g.*, pinhole defects) towards electron-transfer reactions were elucidated with high spatial resolution. By employing 10-20 nm radius Pt SECM tips, it was shown that single spherical NPs (as small as 10 nm in radius) could be resolved,[84] as well as the electrochemical properties of single Pd nanocubes (14 nm sides), as in Figure 1B.[83] Intriguingly, in the latter study, although there was a degree of correlation between the geometry of the nanocubes obtained by SECM and TEM images (compare Figure 1B-i and ii), the sharpness of the electrochemical image, especially at the cube edges, obtained with a constant height scan, cannot be accounted for by considering only the diffusional current at the tip. Other effects were suggested to influence the recorded signal, notably electron tunneling between the tip and surface, although the constancy of the current across the top of a particle would correspond to a remarkably consistent tunneling gap size (Section 5.4).

It is evident from some of these examples that scanning a nanoscale SECM tip within a radius or so distance from a surface with no feedback could be restrictive in terms of the samples that can be imaged. Evidently, without positional feedback, the degree of topographical variation would need to be rather small compared to the tip size, to avoid tip crash, while also noting that the sensitivity and spatial resolution of SECM to surface processes is strongly dependent on the local tip-substrate separation.[32,85] A general lack of independent tip positioning capability in SECM leads to the well-known convolution of topography-reactivity in the electrochemical response. This can be addressed through the use of dual redox

mediators (*i.e.*, one to indicate on topography and the other to measure reactivity)[86] and a very interesting recent approach is to use super-resolution optical imaging to track the tip position, although this requires an optically transparent substrate.[87] An important trend has been the combination of SECM with other SPM methods, such as SICM, scanning tunneling microscopy (STM) or atomic force microscopy (AFM).[44] These hybrid techniques are summarized, and recent developments reviewed in Section 5.

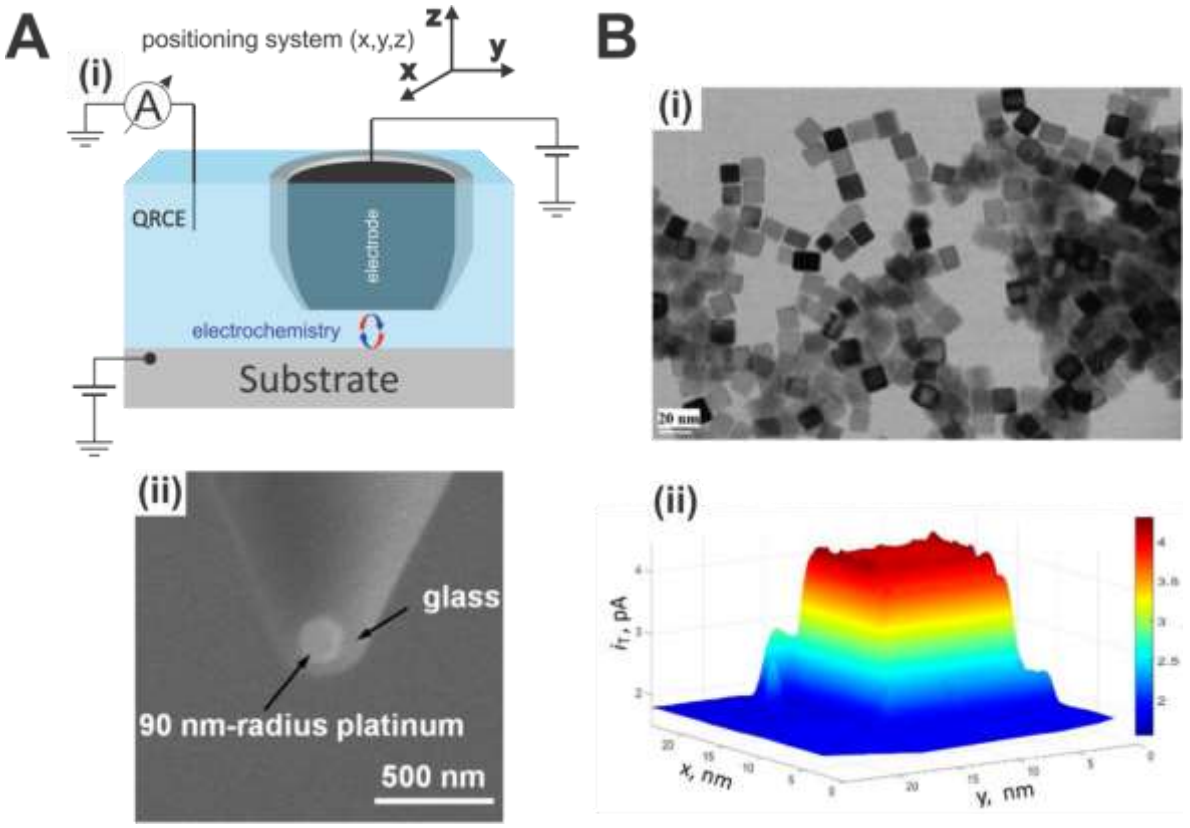

Figure 1. (A) (i) Schematic of a simple SECM setup, highlighting redox shuttling between a substrate and tip electrode. Provided the tip and sample currents are small, a QRCE can be used, rather than individual reference and counter electrodes. **(ii)** SEM image of a FIB-milled, Pt nanoelectrode, used as a SECM tip for single NP electrochemical imaging (reproduced from Kim, J.; Renault, C.; Nioradze, N.; Arroyo-Currás, N.; Leonard, K. C.; Bard, A. J. *J. Am. Chem. Soc.* 2016, 138, 8560-8568 (Ref 63). Copyright 2016 American Chemical Society). **(B) (i)** TEM images of 14 nm sided Pd cubic NPs and **(ii)** positive-feedback electrochemical image of one of the cubes obtained with a 10 nm radius Pt nanoelectrode (SECM tip) in a 1 mM ferrocenemethanol (FcMeOH) solution. Reproduced from Blanchard, P. Y.; Sun, T.; Yu, Y.; Wei, Z.; Matsui, H.; Mirkin, M. V. *Langmuir* 2016, 32, 2500-2508 (Ref 83). Copyright 2016 American Chemical Society.

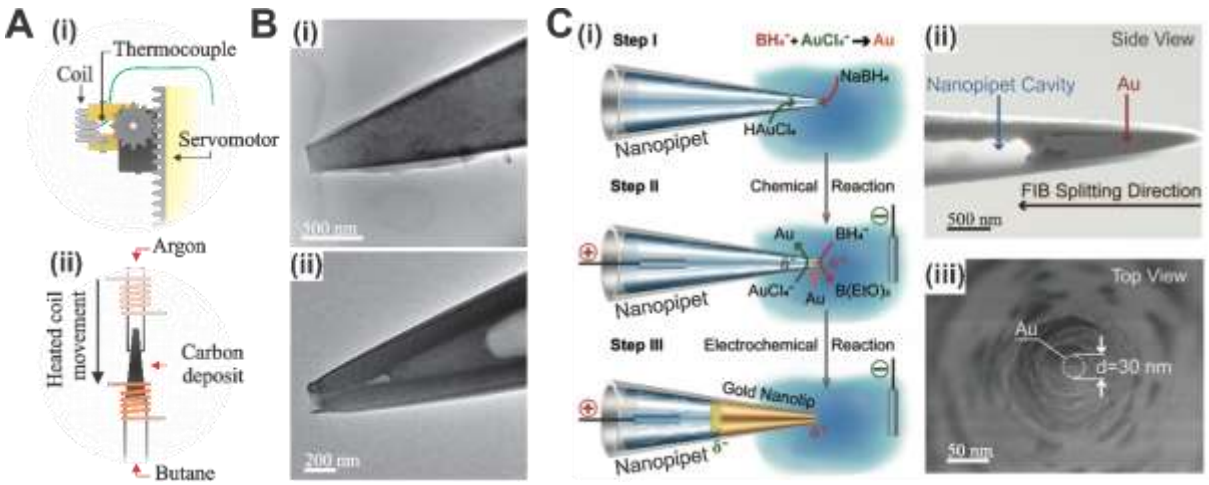

Figure 2. (A) Schematic of an automated heating system employed for the fabrication of carbon nanoelectrodes based on the pyrolysis of butane under an inert (Ar) atmosphere. **(i)** Automation components, such as heating coil, servo motor and thermocouple (for precise temperature control). **(ii)** Coil movement along the nanopipet length resulting in carbon pyrolysis inside the nanopipet bore. Highlighted are Ar and butane inlets and the coil movement direction. **(B)** TEM images of carbon nanoelectrodes fabricated using the automated pyrolysis method. Due to the fine control of the temperature and pyrolysis time, tips can be produced with **(i)** a completely filled carbon layer flush to pipet bore or **(ii)** a hollow carbon layer that can be used as a nano-sampler. (B) was reproduced from Towards Reproducible Fabrication of Nanometre-Sized Carbon Electrodes: Optimisation of Automated Nanoelectrode Fabrication by Means of Transmission Electron Microscopy, Wilde, P.; Quast, T.; Aiyappa, H. B.; Chen, Y.-T.; Botz, A.; Tarnev, T.; Marquitan, M.; Feldhege, S.; Lindner, A.; Andronescu, C.; Schuhmann, W. *ChemElectroChem*, Vol. 5, Issue 11 (Ref 57). Copyright 2018 Wiley. **(C)** Metallic nanoelectrodes fabricated by the bipolar deposition method. **(i)** Schematic representation of the fabrication procedure from the nucleation of the first NP at the pipet bore to the electrochemical deposition and growth of the metallic layer inside the pipet. **(ii)** SEM of a nanoelectrode produced from the bipolar growth method, FIB cut along its length to reveal the depth of the metallic layer growth. **(iii)** SEM top view of a fabricated nanoelectrode. Reproduced from A 30 nm Nanopore Electrode: Facile Fabrication and Direct Insights into the Intrinsic Feature of Single Nanoparticle Collisions, Gao, R.; Ying, Y. L.; Li, Y. J.; Hu, Y. X.; Yu, R. J.; Lin, Y.; Long, Y. T., *Angew. Chem., Int. Ed.*, Vol. 57, Issue 4 (Ref 72). Copyright 2018 Wiley.

3. Scanning Ion Conductance Microscopy (SICM)

3.1 Operational Principles

Traditionally, SICM has been used as a tool for mapping surface topography, most notably for elucidating and tracking morphological changes in soft, living systems, such as biological cells.[88-90] A schematic of the SICM configuration, together with an example topographical map of PC12 cells on a glass slide, is shown in Figure 3A and B. SICM measurements involve bringing a nanopipet filled with an electrolyte solution to the vicinity of a surface of interest. To ensure that there is no contact between the nanopipet and the surface, a bias is applied between a QRCE inserted inside the nanopipet and a second QRCE in bulk solution to generate an ionic current, which is monitored continuously. When the probe is in bulk solution (more than one tip diameter from the substrate), the ionic current is dominated by the nanopipet geometry, nanopipet surface charge, and conductivity of the electrolyte solution.[58] However, when the position of the nanopipet is within one tip (internal) diameter of the surface, the gap resistance between the end of the pipet and the surface influences the current. The conventional view has been that the gap resistance increases, as the nanopipet-substrate distance decreases, leading to a decrease in the ionic current magnitude, typically by around 1-2% percent at practical tip-substrate separations, suitable as a set point for imaging.[6,88] The ionic current can thus be used as a feedback signal to maintain a constant tip-substrate separation as the nanopipet tracks the topography of the substrate, either in a constant distance mode of scanning,[91,92] or more commonly in a hopping/standing approach mode,[93,94] where the tip is approached from bulk solution to the near-surface at each pixel, as depicted in Figure 3C. In this mode, the bulk conductance current can be updated at each pixel, eliminating any issues from drift of the SICM bulk current (should it occur). Topography data is constructed from the z-position of the tip at the set point as a function of *x-y* position in the plane of the substrate. Alternating current (AC) modes of feedback have also been implemented into SICM measurements to improve stability,[91,95,96] but at the expense of scanning speed. The biggest advantage of SICM compared to alternative high-resolution topographical techniques like contact or tapping mode AFM, is that there is no physical contact between the tip and surface, reducing sample damage, particularly for soft samples.[97]

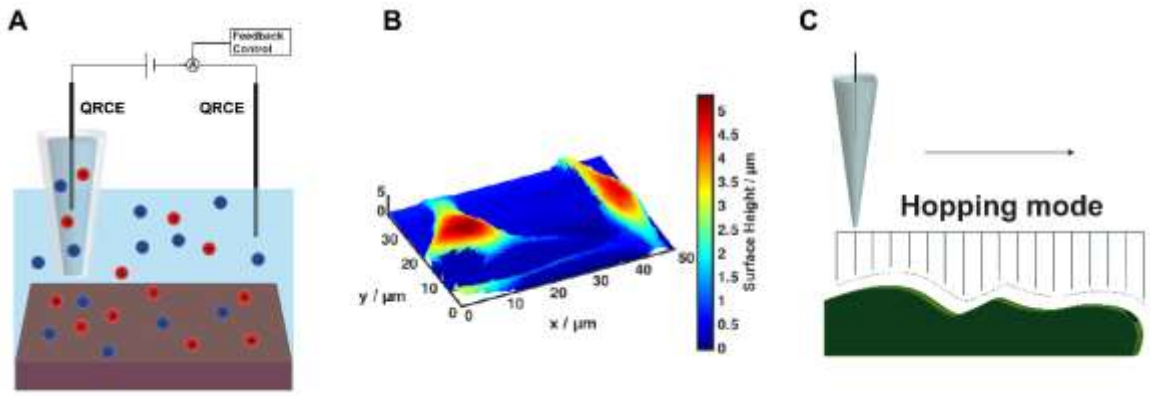

Figure 3. (A) Schematic of a typical SICM setup together with a typical **(B)** SICM topographical map of PC12 cells under physiological conditions. **(C)** Schematic representation of hopping mode scanning with SICM. Reproduced from Page, A.; Perry, D.; Unwin, P. R. *Proc. R. Soc. A* 2017, 473, 20160889 (Ref 6), with permission from the Royal Society of London.

3.2 Functional SICM

Over the past few years, there has been a trend in SICM studies towards simultaneous topography-functional imaging.[6] That SICM can be used to probe surface properties other than topography was evident in the first paper on SICM, where enhanced conductivity was recorded when an SICM probe was over a pore in a porous sample.[89] More recently, the ability to sensitively detect variations in local conductivity has allowed SICM to map substrate surface charge. This was first demonstrated for simple inert substrates in low ionic strength solutions (~10 mM),[98-100] where the Debye length is relatively large (~ 3 nm in aqueous solution).

As with SECM, it is important to address the extent to which the SICM current is sensitive to topography compared to other properties, like surface charge. Finite element method (FEM) simulations have proved particularly powerful for elucidating SICM protocols that can be used to obtain topography and surface charge synchronously and independently.[98-102] In general, when there is a small SICM bias between the two QRCEs, the current is most sensitive to topography, and essentially independent of surface charge.[99] Under these conditions the double layer at the surface is essentially unperturbed by the nanopipet (Figure 4A). At larger biases, however, the edge of the double layer is perturbed and sensed by the significant electric field at the end of the nanopipet (Figure 4B). Further details about mapping surface charge on the nanoscale and more recent developments are outlined below.

3.3 Recent Developments in SICM

There have been interesting recent morphological studies utilizing SICM,[103-106] including the combination of SICM data with co-located images from super-resolution microscopy (although on separate instruments),[107] which build on the established topographical capabilities of SICM. There have also been a number methodological advances, including new scanning regimes and instrumentation, which have resulted in a diversification in the uses of SICM. As highlighted briefly above, modeling is an increasingly important part of SICM studies, allowing experiments to be designed, and quantitative and meaningful information to be extracted from experimental data. Some of the recent progress in each of these areas is outlined below.

3.3.1 Nanoscale Surface Charge Mapping with SICM. Interfacial charge has long been recognized as being of key importance in determining the stability of colloidal systems and in electrochemical processes. Areas where the role of surface charge is gaining increasing focus include ionic crystal growth dynamics and various processes in living (cellular) systems, where key functions such as cellular communication and uptake of nanomaterials are mediated by the charge at the cell membrane.[108,109] The protective properties of some corrosion products on metals are also believed to be linked to the surface charge properties, mediating ion transport during metal degradation,[110] although the literature on this phenomenon is limited,[111,112] mainly due to the difficulty of measuring surface charge on metals directly in corrosive conditions. SICM is emerging as a powerful methodology for surface charge mapping, with wide applicability.[6]

Building on studies in relatively low ionic strength media (mentioned above),[98-100] it has subsequently been shown that surface charge mapping is possible under physiological conditions, where the ionic strength is > 120 mM,[101] as exemplified by synchronous topography (Figure 4C) and surface charge (Figure 4D) mapping of mammalian cells. Several approaches have been taken to elucidate surface charge and topography simultaneously using SICM. Initial studies focused on using AC methods to elucidate topographical and surface charge information.[98,99] The first such approach used a distance-modulated feedback signal, whereby a constant bias was applied between the two QRCEs during nanopipet scanning and the nanopipet was oscillated vertically using a lock-in amplifier (amplitude *ca.* 20 nm, frequency *ca.* 300 Hz). The resulting AC amplitude of the ion conductance current, measured with the lock-in amplifier, was used to set a value for nanopipet positioning. The simultaneously measured ionic current and AC phase signal were then analyzed to reveal surface charge variations. A second approach used bias-modulation,[95] whereby a small harmonic oscillation was applied (lock-in amplifier) about 0 V between the two QRCEs to produce an AC signal

that was detected with the lock-in amplifier and used as a set point to track surface topography. Upon detection of the sample by the tip, the bias between the two electrodes was then swept linearly over a range of a few hundred millivolts, such that the ionic current became sensitive to surface charge. The advantage of this approach is that the contributions of topography (nanopipet-surface distance) and surface charge to the ionic current response are easily discerned. A similar approach has also been used to map the surface charge of polydimethylsiloxane samples that have been patterned with either a positively or negatively charged silane. In this approach, the rectification ratio at the positive and negative potentials of the voltammetric sweep was used to infer the surface charge of the sample.[102]

Most recently, a new approach to charge mapping has been advocated, which greatly speeds up the image acquisition times. This involves bringing the nanopipet near to the sample surface with a bias applied, small enough to render the SICM ionic current to be relatively insensitive to surface charge. Upon detection of the surface through a decrease in the ionic current (increase in gap resistance), a short potential pulse (few 10s of milliseconds duration), of a few hundred millivolts magnitude, is applied such that the ionic current becomes sensitive to surface charge.[113] This approach has been used to map both polymeric surfaces and living cells.[113] An alternative approach has utilized scanning charged samples at two distinct nanopipet biases, one positive and one negative, and considering the difference in the obtained height maps to inform on the effects of surface charge, as demonstrated for model charged phospholipid bilayers.[114] Whilst this approach could sacrifice some accuracy in the topographical information obtained, and requires the near-surface ionic current to be less than the bulk value (which may not always be the case),[98,115] it does allow for faster imaging times and some impressive images have been reported.[114]

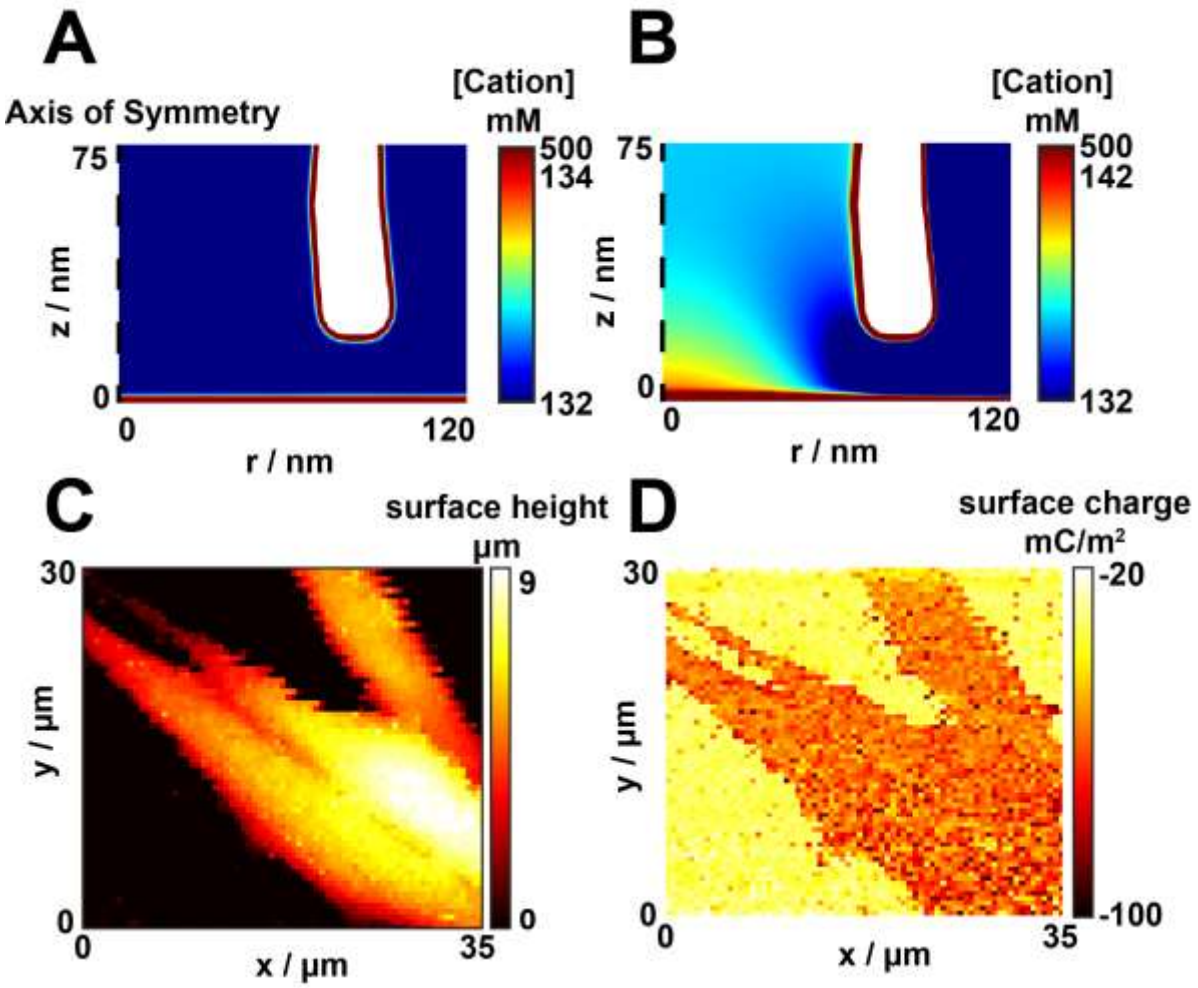

Figure 4. Simulated cation (K^+) concentration under physiological conditions (~140 mM 1:1 electrolyte) near a charged interface (-80 mC/m^2) with an applied tip bias of **(A)** -50 mV and **(B)** 400 mV. These images are of the axisymmetric cylindrical geometry (that defines the tip-surface geometry and reduces the simulation problem to 2D).[116] **(C)** Topographical and **(D)** surface charge maps of PC12 cells under physiological conditions obtained synchronously in a single scan using differential concentration SICM. Adapted from Perry, D.; Page, A.; Chen, B.; Frenguelli, B. G.; Unwin, P. R. *Anal. Chem.* 2017, 89, 12458-12465 (Ref 116). Copyright 2017, American Chemical Society.

FEM simulations (typically carried out using the COMSOL Multiphysics software package) are essential in order to extract quantitative information from the experimental data. These simulations typically solve simultaneously the Poisson, Nernst-Planck and the Navier-Stokes equations to determine the concentrations, electric field and electroosmotic flow, respectively, in nanopipet (SICM) systems.[6,100,116] An important aspect to modeling the SICM

response is knowing the nanopipet geometry accurately, and significant advances in probe characterization (making use of TEM and current-voltage measurements) have come about in recent years, allowing for more realistic simulations of SICM data.[58,117]

3.3.2 Nanoscale Electrochemical Flux Mapping. A new avenue for SICM is as a tool for mapping electrochemical fluxes at electrode surfaces on the nanoscale. Electrochemical processes are accompanied by changes in the ionic environment near the electrode surface, and so the proven ability of SICM to probe local solution conductivity quantitatively offers considerable prospects for visualizing electrode activity. A handful of studies, thus far, demonstrate different approaches and the great promise of SICM as a powerful tool to elucidate structure-activity relationships at electrochemical interfaces.

SICM reactivity mapping has been demonstrated in 2 different approaches, applied to: (i) hydrazine oxidation and the hydrogen evolution reaction (HER); and (ii) the oxidation of ferrocenemethyl trimethylammonium ($FcTMA^+$) hexafluorophosphate, both at a platinum UME.[118] A hopping voltammetric approach was used to investigate the oxidation of hydrazine and HER, whereby the SICM tip approached the substrate electrode surface at a potential where there was no reaction (to map out the topography) and then the substrate potential was scanned linearly to oxidize hydrazine and then reversed to cathodic potentials to drive HER, both processes causing changed in local ionic conductivity that were sensed by the SICM tip. This voltammetric process was repeated at a series of pixels to create a dataset that could be reconstructed as a potentiodynamic movie of ion conductance maps as a function of substrate electrode potential. For $FcTMA^+$ electro-oxidation, a distance modulated approach was used to sense the surface and obtain topographical information using an Archimedes spiral scan profile to enhance the data acquisition rate. The topographical data were then used to set the path of the tip during subsequent high-speed SICM reaction imaging, such that images of 16,000 pixels were obtained every 4 seconds, for a range of different potentials, with the tip position automatically adjusted to maintain a constant tip-substrate separation in the course of the scans. Data were presented as potentiodynamic movies of the nanopipet ionic current over the area of interest as a function of driving potential (time). For both experimental strategies, the movies highlighted clearly that there was a conductivity change around the UME as the reactions progressed, as shown in the example images from the movie for $FcTMA^+$ oxidation in Figure 5A.[118]

A subsequent approach used a 30 nm diameter nanopipet and a DC ionic current self-referencing hopping format, with a pulsed potential program applied to the substrate so as to probe the surface topography and electrochemical reaction rate synchronously (Figure 5B shows example data). At each pixel in the image, the SICM probe was brought into the vicinity of the sample (to map the topography), with the electrode reaction "off" and a driving potential was then applied to the substrate, which was either an Au UME or a carbon fiber UME with electrodeposited catalytic AuNPs, to drive borohydride oxidation. Borohydride oxidation results in significant depletion of the concentration of hydroxide ions, drastically reducing the local conductivity of the solution, which was sensed by the SICM tip.[119] By combining experimental data, such as the representative examples in Figure 5B, with FEM simulations, several interesting phenomena were observed. At low driving potentials for the oxidation, a halo effect in conductivity around the NPs was apparent, due to depletion of ions in the gap present between the NPs and the inert support. At higher driving potentials the region around each NP was seen to be depleted.

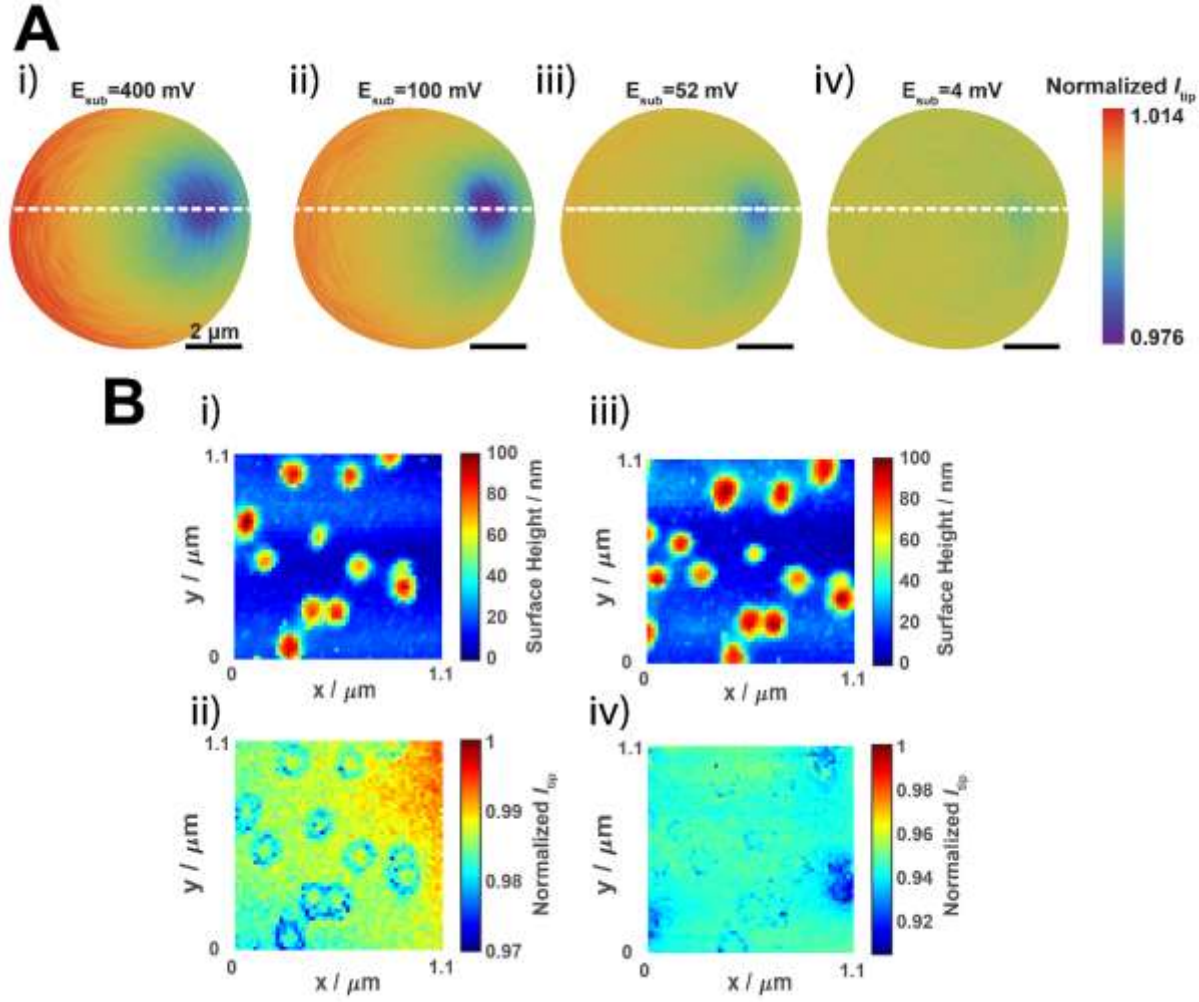

Figure 5. (A) Fast spiral scanning SICM reaction mapping of $FCTMA^+$ oxidation at a 430 nm radius Pt UME sealed in quartz, with images at different applied potentials (vs. Ag/AgCl QRCE) shown in (i-iv). Reproduced from Momotenko, D.; McKelvey, K.; Kang, M.; Meloni, G. N.; Unwin, P. R. *Anal. Chem.* 2016, 88, 2838-2846 (Ref 118). Copyright 2016, American Chemical Society. **(B)** Synchronous topographical and reaction mapping of borohydride oxidation at AuNPs on a carbon fiber support. Topographical maps (i,iii) and normalized ionic current maps (ii,iv) obtained at low (i,ii) and high (iii,iv) driving potential. Experiments were performed in 3 mM $NaBH_4$ and 30 mM NaOH. Reproduced from Kang, M.; Perry, D.; Bentley, C. L.; West, G.; Page, A.; Unwin, P. R. *ACS Nano* 2017, 11, 9525-9535 (Ref 119). Copyright 2017, American Chemical Society.

Dopamine oxidation at a carbon fiber electrode has also been visualized using SICM.[116] In these studies, dopamine was present in the SICM tip but not in the bulk solution, and dopamine was dispensed from the nanopipet at a constant rate during the course of the scan

(hopping mode) using a fixed delivery potential applied to the SICM QRCE. Upon the nanopipet detecting the surface, through a decrease in the ionic current, the substrate potential was swept linearly from an initial value where there was no reaction to a value whereby dopamine oxidation was driven at a diffusion-limited rate, with the resulting ionic current maps and movies, as a function of potential, revealing the activity around the carbon fiber electrode.

There are several potential advantages to operating SICM with a different composition in the tip to that in solution, referred to as differential concentration[116] or biphasic SICM.[120] An enhanced sensitivity to surface charge can be achieved,[116] and enhanced spatially-resolved reactivity mapping results when the electroactive species is delivered from the nanopipet and is not present in the bulk. This approach to reaction mapping is particularly beneficial in cases where the substrate electrode can easily be fouled by the electrochemical process of interest (such as is the case for dopamine electro-oxidation at carbon electrodes[121]), because the reaction is only "on" in the part of the substrate in the vicinity of the tip where reagent is delivered. Experiments and modeling under differential concentration conditions have highlighted the importance of the different QRCE equilibrium potentials in the tip and bath, and also how electroosmotic flow can influence the SICM response.[116] These developments make the modeling of SICM mass-transport increasingly robust and comprehensive.

3.3.3 Other Applications of SICM. To enhance the functional capability and selectivity of SICM, there have been several attempts to incorporate biological pores at the end of SICM nanopipets. A lipid bilayer, with a GΩ resistance seal, can be formed across the nanopipet opening and a single (or several) α-haemolysin pore(s) can be inserted into the bilayer, with successful insertion indicated by an ionic current flow across the membrane, with an applied bias.[122,123] Such channels then allow for specific molecular detection, to the single molecule level, by monitoring the current for binding events. For example, as a single β-cyclodextrin molecule binds to a α-haemolysin protein channel, the pore becomes blocked, and a decrease in the ionic current is observed.[123] Similarly, a dual-barreled probe has been utilized, where one channel was kept open for SICM probe positioning, whilst a lipid membrane from a donor cell, which contained ligand-gated ion channels, was attached across the opening of the second channel. Positioning the probe near a source for the specific ligand, such as Ca^{2+} ions, led to an increased probability of pores being open, resulting in an enhanced current through the pore.[122]

Another significant recent development using modified SICM probes for molecular detection, has led to a novel glucose sensor, capable of detecting the intra-cellular glucose concentrations present in target single cells.[124] The inside of the end of a nanopipet was coated with poly-L-lysine and a cross-linking agent used to immobilize glucose oxidase onto the inner surface of the nanopipet probe. When the device was in a glucose-containing medium, the enzyme catalyzed the oxidation of β-D-glucose to D-gluconic acid, resulting in a change of the conductance of the probe, which could be sensed as a current flow under bias. This approach has been used to measure the intra-cellular concentration of glucose in different cell phenotypes, with cancerous and non-cancerous cells being distinguishable.

A more recent SICM configuration that has shown great promise for simultaneous topography and conductance measurements across biological membranes, is potentiometric SICM (P-SICM). The probe is a dual-barreled theta pipet, with one channel providing traditional SICM feedback for positioning and topography mapping, and the second channel measures the local potential. Initially applied to model nanopores in polymer membranes and to explore channel conductance at tight junctions,[125-127] this technique has recently been used to identify and probe the different conductance pathways in bi- and tri-cellular junctions in epithelial membranes, which is a particularly exciting development.[128]

3.3.4 Methodological Advances. It is also useful to briefly highlight significant recent advances that have been made to improve SICM equipment or implement novel scanning regimes that may have exciting applications in future. Usually the SICM nanopipet probe is brought towards the sample in a normal (perpendicular) direction, but lifting this restriction by mounting the nanopipet on a patch-clamp micromanipulator could be advantageous for some applications, in a mode termed angular approach SICM.[129] This approach opens up the possibility of mapping regions of cells, not accessible with standard SICM approach modes including the sides of stereocilia.[129]

In hopping mode, the SICM tip is retracted a fixed distance away from the surface at each pixel before being moved laterally, and usually this distance is determined by the height and steepness of the sample being probed.[94] The retract distance employed is a limiting factor on SICM scan times and so methods that reduce this are advantageous. Recently, SICM feedback control during the lateral movement across the sample has been considered,[130] which allows smaller retract distances to be used.

Typical SICM scans tend to focus on a narrow region of a sample of a few square microns but there have been several recent studies focused on increasing the range of length scales that can be probed with SICM through new approaches to image processing,[131] combining nanoscale precision piezoelectric positioners with shear force actuators[132] or using micropositioner stages capable of ranges of 10s of millimetres.[133] These approaches increase the range of samples that can be probed and open up exciting new applications for SICM on the macroscale with, for example, whole fingerprints being imaged.[133] If combined with the functional capabilities of SICM, this new approach could open up new avenues in forensic science, for example. With higher speed imaging of increasing focus and attention, the recent development of a high speed tip-scanning stage for SICM is particularly noteworthy.[134]

Finally, in addition to those mentioned above, there have been further attempts to improve FEM modeling of SICM experiments. One notable attempt combines experimental and simulated approach curves as a means of non-destructively obtaining information about the probe geometry.[135] However, this work has limitations in that the probe was considered to be purely conical in shape and surface charge effects on the approach curves were not included in the model. Whilst there is value in a facile means of approximating the probe geometry, TEM characterization is preferable, where possible, if quantification of SICM data to obtain functional information is to be attempted.[58]

4. Electrochemical - Scanning Tunneling Microscopy (EC-STM)

4.1 Development and Operational Principles

Since its inception, STM[136] has proven to be extremely powerful for studying surface topography and electronic structure down to the atomic level, including in electrochemical environments.[137] The core operating principle of STM involves the approach of an extremely (atomically) sharp metallic tip into close proximity to a conducting sample surface, with a bias applied between the two. Once the tip is sufficiently close, electron tunneling occurs, with the magnitude of the resulting tunneling current being exponentially dependent on the tip-sample separation. Most commonly, STM is operated in a "constant current" mode (see Figure 6A), where the measured current is kept constant by adjusting the position of the tip. During operation, the *z*-positional adjustment is measured as the tip is scanned across the sample, allowing maps of the sample topography to be produced. It should be noted that care must be taken when interpreting STM images, as the tunneling current is also sensitive to the local

density of states and not just tip-substrate distance (*i.e.*, topography). In comparison to alternative newer *in situ* methods, such as electrochemical liquid cell TEM,[138] there has been something of a decline in interest in EC-STM. However, recent innovations which we consider here, should rekindle interest and lead to the increased use of EC-STM.

4.2 Combined Voltammetry and EC-STM Studies

A key attribute of *in situ* EC-STM is the ability to track changes in surface topography during voltammetry. Although this is a well-known use of EC-STM, several recent studies illustrate the considerable information that can be obtained. As an example, the potential dependence of anion intercalation into HOPG in 4 different acidic electrolytes (HCl, $HClO_4$, H_2SO_4 and H_3PO_4) has been investigated.[139] At oxidizing (positive) potentials, anion intercalation in $HClO_4$ and H_2SO_4 were shown to result in the formation of surface "blisters", not observed in the other electrolytes. The first stages of the intercalation involved the erosion of terraces, locally damaging the surface *via* formation of holes, new edges, terraces and vertices. This study also demonstrated how the intercalation process may limit the quality and size of exfoliated graphene sheets, due to progressive damage to the surface.[139] The potential dependence of germanene growth on Au(111) showed that initial deposition occurred at defects in the well-documented Au(111) herringbone reconstruction. This structure was then relaxed by further growth in the troughs of the face-centered cubic surface. Finally, any further growth created a second layer of small, weakly bound islands before further lateral growth.[140]

In situ EC-STM has considerable potential for examining energy materials. The oxygen reduction reaction (ORR) catalyzed by iron-pthalocyanine (FePc) layers adsorbed on Au(111) was recently studied using EC-STM, [141] with images suggesting the formation of the FePc-O_2 complex. The electrochemical roughening of a Pt(111) surface when potential-cycled (between 0.05 V and 1.35 V vs. the reversible hydrogen electrode, RHE) in $HClO_4$ media has also been elucidated with EC-STM, with the potential held in the double layer region (0.4 V vs. RHE) to record a series of STM images as a function of the number of cycles, in order to track morphological changes ("roughening") induced by oxide formation/stripping. Two different roughening regimes were identified, a "nucleation and early growth" regime followed by a "late growth" regime. The first stage showed the formation of an increasing number of nanoscale islands, which increased in radius and slightly in height with potential cycling. Interestingly, while the step sites created during the early regime contributed to the surface roughness, they did not contribute to the voltammetric signal. The second (late) regime

commenced once the islands coalesced, resulting in island growth in predominantly the *z*-dimension (height), which contributed strongly to the voltammetric signal and continued up to at least 170 voltammetric cycles.[142] A follow up study from the same group used electrochemical – AFM to study the same process but on polycrystalline Pt. The use of this technique allowed for a wider potential window to be applied (0.05 – 2.5 V), as EC-STM normally has an upper limit of 1.3 V (extensive oxide film formation) due to conductivity requirements. The wider potential window used and the polycrystalline nature of the sample led to a different roughening mechanism. The roughening up to 1.5 V previously observed was not seen (possibly due to the polycrystalline nature of the sample, as well as the reduced resolution of the AFM), but the surface was instead roughened above 1.8 V through the formation of PtNPs.[143]

A combined ultrahigh vacuum (UHV)-electrochemistry set-up has been developed that facilitates the preparation and structural characterization of complex nanostructured electrode surfaces under UHV by STM, and electrode transfer under clean conditions for electrochemical measurements in a flow cell, including the provision for differential electrochemical mass spectrometry measurements and the use of collector electrodes to allow product analysis. This set up was employed to demonstrate the differences in electrochemical (electrocatalytic) properties in two systems: ORR on Pt_xAg_{1-x}/Pt(111) monolayer surface alloys and bulk CO oxidation on Pt monolayer island modified Ru(001) surfaces. In both cases, potential-dependent surface restructuring (traced with STM), altered the electrochemical signal and electrocatalytic properties.[144]

4.3 High Speed STM

While several factors impact the speed at which STM images can be acquired, the limiting factor is generally the feedback used for "constant current" mode imaging (Figure 6A). While the "constant height" mode (Figure 6B) is only effective on very flat samples and contrast will be lost in any areas beneath the main imaging plane, it can be carried out much faster than imaging in the conventional constant current mode.[145,146]

Recently, high-speed (constant height) EC-STM was utilized to image the surface dynamics of Au(111) crystals in three different ionic liquids. Each STM frame was obtained on a timescale of *ca.* 100 ms, allowing atomic scale changes in the surface to be traced on the electrochemical timescale. Potential sweeps of the surface showed that for all three ionic liquids, there was a similar potential dependency of the arrangement of adsorbed cations

(imidazolium and pyrrolidinium cations explored). Near the potential of zero charge, interfacial ions are highly mobile, but when the potential was swept cathodically a sequence of ordered adlayers was observed. Cations adsorbed parallel to the surface formed a first stripe-like phase, and as the potential was reduced further an almost square in-plane structured adlayer was formed.[145] A study from the same group investigated the microscopic mechanisms of Bi electrodeposition on Au(111) and Au(100) surfaces. Using high-speed STM, real time videos of atomic movement were obtained, in which Bi-Bi bond formation was shown to govern the epitaxial growth of the Bi deposits in an electrochemical environment, as shown in Figure 6C. This study also demonstrated the (electrochemical) formation of truly one dimensional Bi nanowires on the Au(111) surface.[146]

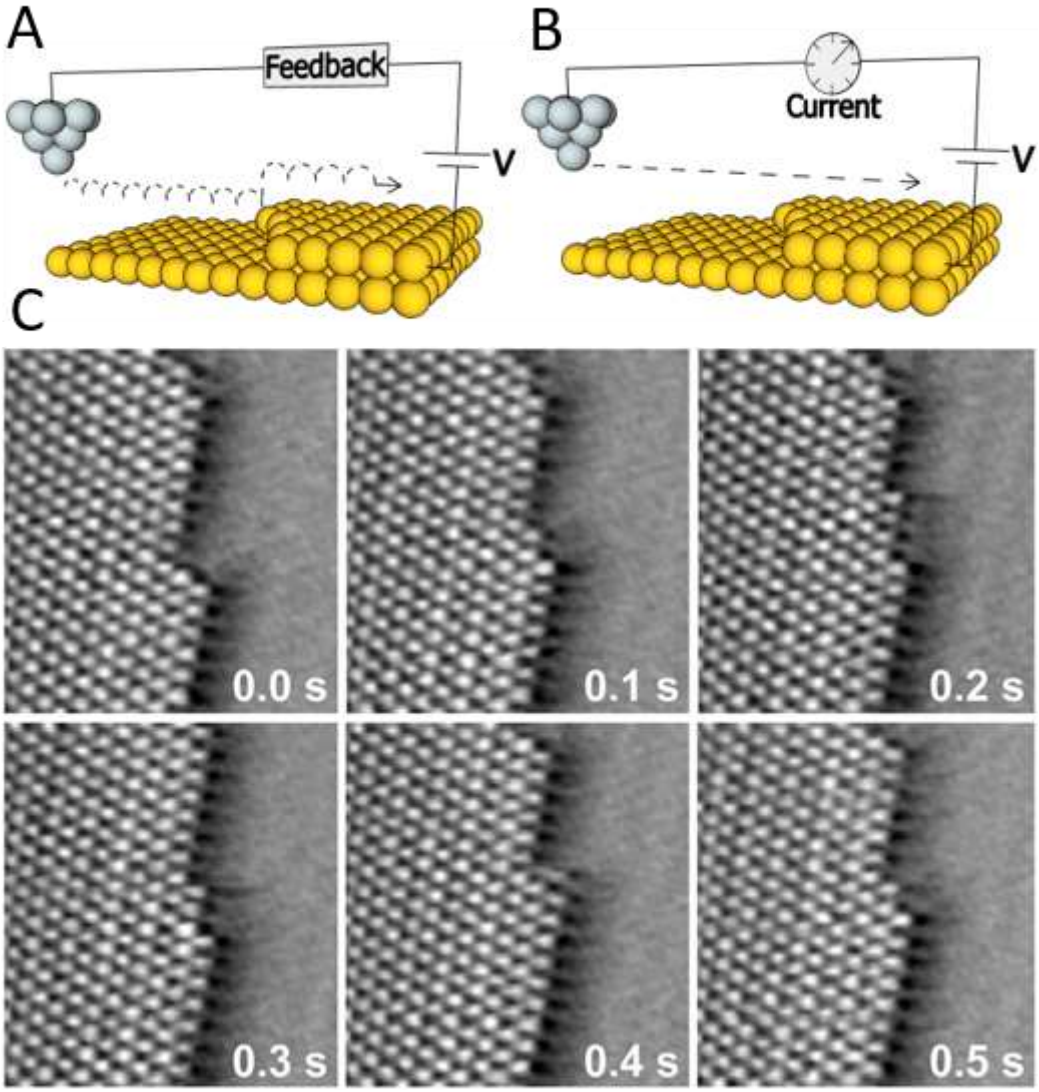

Figure 6. (A) Representation of the more commonly used constant current imaging mode in STM, where a feedback loop controls the position of the tip to keep tunneling current constant.

(B) Constant height imaging mode used in (C), where the vertical position of the tip is kept constant and the tunneling current is measured. **(C)** Sequence of STM images taken in 100 ms intervals of Bi deposits on a Au(100) surface. Atomic resolution of kink propagation along the island edge is displayed. Scan range of (75×70 Å^2). (C) was reproduced from Matsushima, H.; Lin, S. W.; Morin, S.; Magnussen, O. M. *Faraday Discuss.* 2016, 193, 171-185 (Ref 146), with permission from the Royal Society of Chemistry.

4.4 STM Faradaic Noise Analysis

Faradaic currents are minimized at the STM tip in order to improve the signal-to-noise in EC-STM images, however, if analyzed appropriately, it has been shown that the faradaic noise in the tunneling current can provide useful information about electrochemical (electrocatalytic) activity. This approach was demonstrated in a recent pioneering study, where, using a conventional EC-STM setup, the faradaic noise in the tunneling current whilst scanning a Pt(111) surface in aqueous $HClO_4$ was monitored and used to derive information regarding the location of active catalytic sites. It was shown that when the potential of the sample was changed to a region where HER occurred, locally increased noise levels were observed over surface features such as steps. The increase in the tunneling current noise was reasonably attributed to enhanced catalytic activity, which can be explained by the faradaic processes altering the local solution composition, which in turn affects the tunneling barrier between the tip and the sample. The same idea was applied to HER at Pd islands of monoatomic thickness on a Au(111) surface (Figure 7A) and, once again, an increase in noise was observed over the Pd compared to the Au(111) surface (Figure 7B), in agreement with the relative HER activities of these materials. More interestingly, greater tunneling current noise was observed at the boundary between the Pd islands and Au(111) surface (Figure 7C and D), attributed to a greater catalytic activity at the boundary, suggesting that maximizing Pd boundary atoms could increase the macroscopic catalytic activity of the system. Whilst not completely quantitative, this novel approach has demonstrated the ability of conventional EC-STM to elucidate the relative contributions of different surface active sites to the overall catalytic activity of macroscopic surfaces.[147]

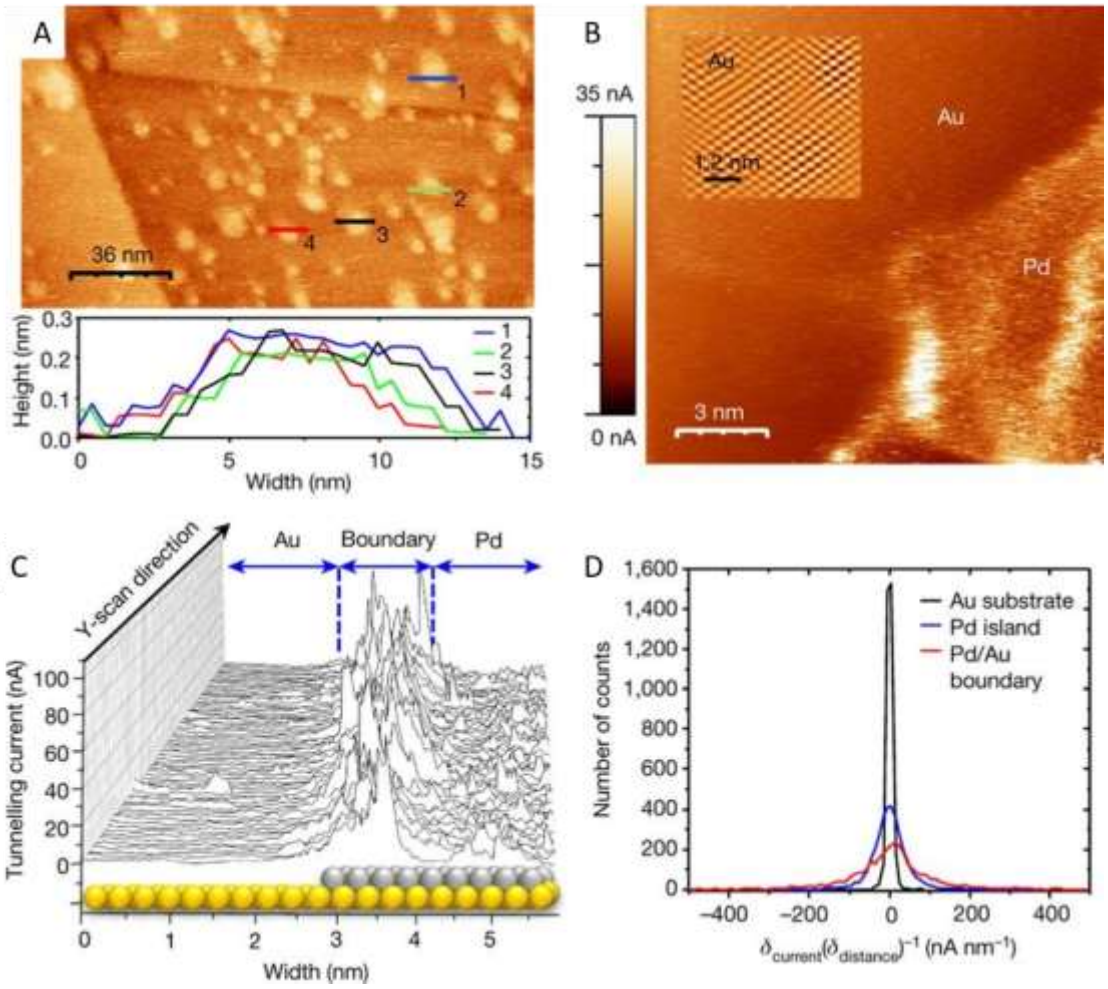

Figure 7. (**A)** In air STM scan of Pd islands on an Au(111) surface with line profiles to display monoatomic height. (**B)** Constant height STM image of Pd island and Au surface boundary under HER conditions (0.1 M H_2SO_4). Inset of atomically resolved Au surface via fast Fourier transform analysis. (**C)** STM line scans from **B**, showing increased noise and hence catalytic activity over the first few Pd atoms of the Au-Pd boundary. (**D**) Statistical current derivatives of STM line scans in **C**, displaying increased noise over the Pd island and a further increased noise over the Pd/Au boundary. Reprinted with permission from Springer Nature: *Nature* (Ref 147) (Direct instrumental identification of catalytically active surface sites) by (Pfisterer, J. H. K.; Liang, Y.; Schneider, O.; Bandarenka, A. S.), COPYRIGHT (2017).

5. Hybrid SEPM Techniques

Above, we have considered some of the key developments in SECM, SICM and EC-STM that have enabled these techniques to address electrochemical interfaces at the nanoscale. Each methodology has particular attributes that guide usage. Hybrid SEPM techniques seek to

combine the merits of different SEPMs and SPMs to provide a more holistic view of interfacial structure-properties-activity.

5.1 SECM-SICM

Of the hybrid SEPM techniques, the combination of SECM and SICM, termed SECM-SICM (or SICM-SECM),[88,97] is particularly powerful. Most commonly, probes suitable for SECM-SICM can be constructed using a dual-barreled theta pipet, with one open channel for precise tip positioning and topographical mapping using SICM feedback, and the second channel containing a solid electrode for SECM sensing (Figure 8A-i).[70]

The considerable capability of SECM-SICM is demonstrated by mapping of topography simultaneously with molecular uptake across the cell wall of living *Zea mays* root hair cells (Figure 8A-ii and 8A-iii).[148] The SICM channel was used to both map topography and deliver a target molecule of interest, $[Ru(NH_3)_6]^{3+}$, by loading the tip with $[Ru(NH_3)_6]^{3+}$ and applying a positive tip bias to promote delivery. The corresponding uptake was quantified by amperometric detection of $[Ru(NH_3)_6]^{3+}$ at the SECM channel (by diffusion-limited reduction). A key aspect of this study was the use of a self-referencing strategy, in which the response of both the SICM and SECM channels were updated in bulk solution at each pixel in images that were obtained in a hopping mode (see Figure 3C). This was particularly important for the SECM channel because, in common with many amperometric electrodes employed for cellular analysis, its response deteriorated during the course of a scan, but this could be fully accounted for by referencing the near surface SECM current to the corresponding updated value for bulk solution. With this approach, uptake can be monitored quantitatively, because as the SECM-SICM probe is approached towards a sample, into which the species, $[Ru(NH_3)_6]^{3+}$, can pass from the SICM channel, there is a decrease in the electrochemical signal at the SECM channel compared to that in bulk solution (SECM tip detection in competition with cellular uptake). In contrast, over an inert sample (*i.e.*, an impermeable surface), there is an increased current at the SECM channel, as the mass-transport from the open (SICM) channel becomes restricted, compared to when the probe is in bulk solution, and a higher flux results at the amperometric electrode. Enhanced uptake rates were measured at the tip of the cells, where the SECM current was lower (Figure 8A-iii). It is interesting to note that differences in cellular uptake between the tip and body of *Zea mays* root hair cells correlated with surface charge variations previously identified from SICM surface charge mapping experiments (Section 3.3.1).[101]

SICM-SECM has been utilized further, combining the ionic and electrochemical currents recorded at the dual-channel probe, to infer on the spatial ion concentration profile and chemical fluxes, around either an unbiased electrode or near a cell membrane.[149] For the substrate electrode case, this approach allowed the kinetics of redox mediator regeneration to be probed. In the case of cell imaging, heterogeneous permeability of and adipocyte cell membrane to ferrocene methanol ($FcCH_2OH$), a hydrophobic redox-active probe molecule that can hence cross the membrane, could be observed. The SECM probe was held at a potential to drive the oxidation of $FcCH_2OH$ and so could be used as a measure of the local $FcCH_2OH$ concentration.

5.2 AFM-SECM

AFM has been effectively coupled with other techniques to produce multifunctional capabilities for high-resolution imaging.[47] The coupling of AFM and SECM was reported almost 2 decades ago,[150,151] and tips and instrumentation for AFM-SECM are now available commercially, which should increase the number of groups using this technique and diversify applications. Using specially designed SECM-AFM cantilever tips electrochemical, topographical and mechanical information of the substrate can be acquired simultaneously.[152-154] Such a hybrid approach, relying on the capability of SECM for probing the electroactivity (or chemical fluxes) and of AFM for topography and substrate mechanical properties, can be extremely useful for investigating soft electronic devices, such as implantable and wearable electrodes or flexible lab-on-a-chip devices.[155]

A design that incorporates a conical nanoscale electrode on the end of an AFM tip has recently been introduced, thoroughly characterized, and applied to several systems to highlight the versatility of AFM-SECM imaging,[153,156] including mapping electrochemistry of outer sphere redox reactions at HOPG, where high activity of the basal plane was observed, in line with macroscopic[157] and nanoscopic measurements from other electrochemical imaging techniques.[158] Conical tips have also being employed for imaging, with high spatial resolution, the flux of $[Ru(NH_3)_6]^{3+}$ through silicon nitride nanopore arrays with different pore-pitch spacing allowing the *in situ* visualization of the radial diffusion across the nanopores and how pore pitch can impact the diffusion profiles at the nanoscale.[159] 50 nm radius Pt disk electrodes, attached to quartz tuning forks, have been used as AFM-SECM tips and employed for the acquisition of high-resolution electrochemical images (in tandem with topography) of intricate

substrates. The geometry of these tips (much closer to a conventional SECM electrode) facilitates the quantitative analysis of the electrochemical response.[160]

Despite an apparently small trade-off in resolution when compared to the highest standalone SECM studies employing nanoscale-sized electrodes, it is clear that the integration of SECM with AFM brings a clear advantage over SECM alone, as it neatly solves the topography/activity conundrum, mentioned above in Section 2.1, and allows a much greater diversity of substrate topography to be tackled than possible with SECM constant height imaging. Not surprisingly many standalone applications of AFM or SECM are now being revisited with AFM-SECM. Corrosion processes, for instance, can now be accessed *in situ* by monitoring both topographical changes on the substrate and by electrochemically detecting oxidation products of the corrosion process and/or substrate passivation, providing deeper insight on the corrosion process.[161]

The use of AFM in tandem with SECM allowed AFM-SECM to be employed as a read-out of microarray-based sensing systems. Such devices are often employed for important biological screenings (such as enzyme-linked immunosorbent assay) and often rely on fluorescence techniques as read-out. Despite the high sensitivity, the lateral resolution of fluorescence read-out is diffraction-limited. By employing molecule touching-AFM,[162] where the tip is functionalized with redox active molecules, rather than the redox molecules being in solution, AFM-SECM has been used as a high throughput serial read-out technique for imaging high density molecular nanoarrays.[163] Owing to the flexible chemical detection capabilities of SECM, many applications of AFM-SECM as a bioanalytical sensing tool or in the study of biologically relevant samples have being reported, such as screening immunocomplexes anchored to single viral particles,[164,165] and investigations of the insertion of protein pores into supported lipid membranes, an important cell membrane model.[166] AFM-SECM (and its diverse modes of operation) will undoubtedly find further use on biologically relevant samples (much like SECM-SICM, described in Section 5.1) especially considering further efforts towards the development of AFM-SECM capability, such as conductive colloidal probes recently reported.[167]

AFM-SECM and conducting AFM tips will be employed increasingly to probe the activity and function of energy materials. There was a very interesting recent report on the direct, *in operando,* measurement of the electrochemical potential of electrocatalysts, by using an SECM-AFM tip as a local potential sensing device.[168] The use of AFM to monitor

topographical and volume changes in energy materials during operation is a very powerful application,[169] and one can envisage how these types of study would be further enhanced with AFM-SECM.

5.3 AFM-SICM

A recent AFM-SICM hybrid technique using a commercial AFM probe (for topography) with a fluid channel for conductance measurements has been implemented for high speed charge mapping (Figure 8B-i).[170] This approach uses the force based feedback of AFM for mapping topography, whilst simultaneously recording the ionic current through the open pore of the AFM tip (as in SICM) to infer on surface charge (Figure 8B-ii and 8B-iii). The approach builds on earlier applications of the so-called Fluid-Force Microscopy (FluidFM) technique for simultaneous AFM-SICM measurements.[171,172] This approach shows great promise for mapping surface charge at "hard" materials and speeds up the image acquisition process compared to present SICM charge mapping methods (Section 3.3.1). More work is needed to determine whether this approach can be extended to soft, living systems, without causing sample damage, and whether small orifice sizes that compete with the 30 nm presently achievable with SICM will be possible in AFM-SICM.[119] This hybrid approach has also been employed to modify substrates in a nano-fabrication approach where the chemical-solution delivery capabilities of SICM[116,173] are combined with the topographical sensing capabilities of AFM to "print" patterns and structures over the substrate surface in a very precise and controlled fashion.[174]

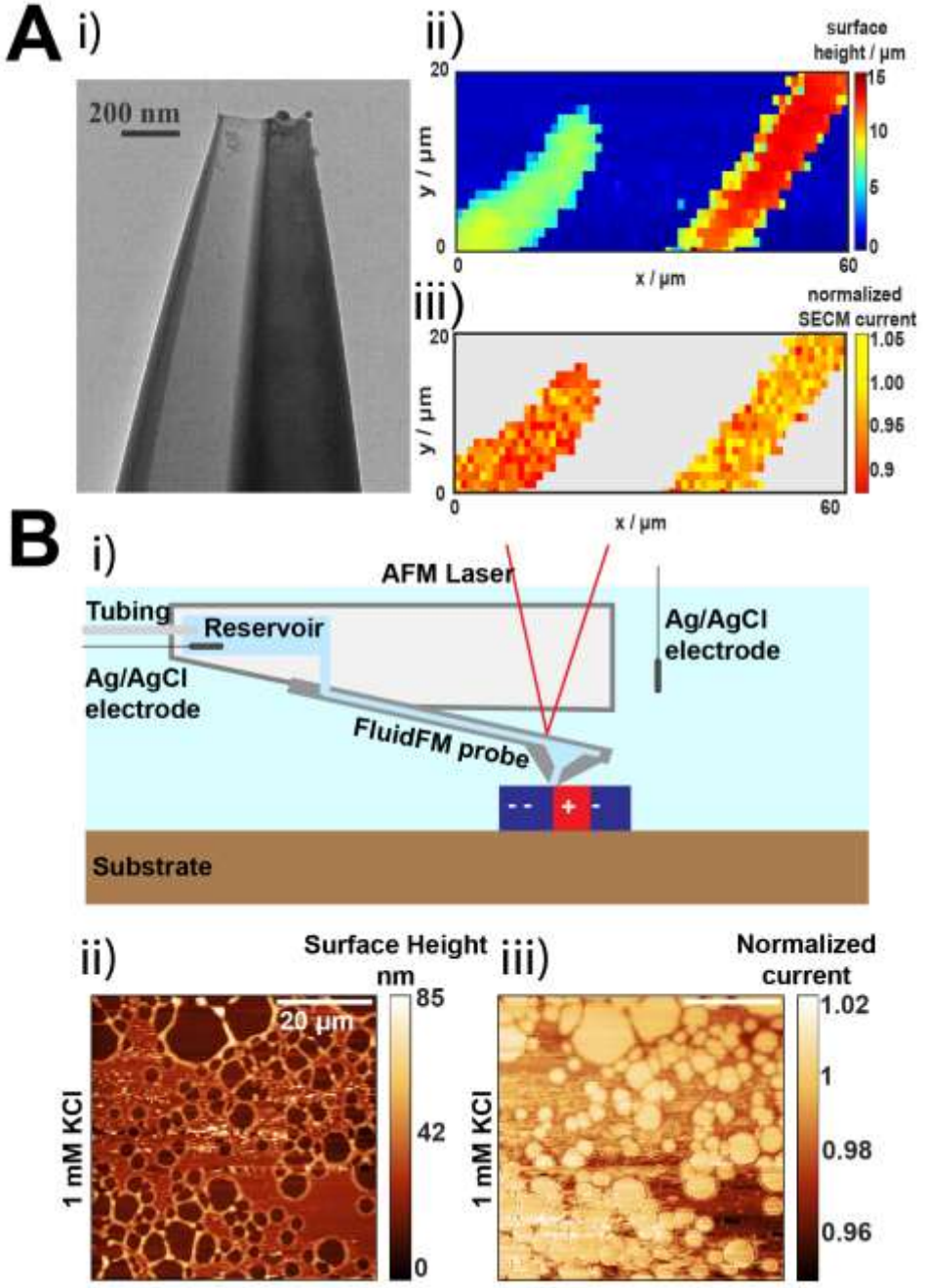

Figure 8. (A) (i) TEM image of a typical SICM-SECM probe, with one open channel (SICM) and one channel containing pyrolytically deposited carbon (for SECM). Simultaneous topography **(ii)** and molecular uptake maps **(iii)** of a root hair cell, monitored through using the SECM channel current (lower current magnitude values corresponding to higher uptake rates). The open SICM channel contained 10 mM $[Ru(NH_3)_6]^{3+}$ which was delivered through the application of a positive tip QRCE potential. Adapted from Page, A.; Kang, M.; Armitstead, A.; Perry, D.; Unwin, P. R. *Anal. Chem.* 2017, 89, 3021-3028 (Ref 148). Copyright 2017,

American Chemical Society. **(B)** Surface charge mapping with combined AFM-SICM, carried out using a FluidFM probe that contains an open channel, through which an ionic current is measured with 2 QRCEs. Schematic of setup shown in **(i)** together with simultaneously obtained **(ii)** topography and **(iii)** normalized current (proxy for surface charge) maps of an interrupted polystyrene film on glass in 1 mM KCl. Adapted from Dorwling-Carter, L.; Aramesh, M.; Han, H.; Zambelli, T.; Momotenko, D. *Anal. Chem.* 2018, 90, 11453-11460 (Ref 170). Copyright 2018 American Chemical Society.

5.4 STM-SECM

The idea of STM-SECM is to be able to make high-resolution topography maps (STM mode) and electrochemical maps (SECM mode) from the same nanoscale metallic probe (insulated except at the very end). One of the first attempts at combined STM-SECM took STM scans of PdNPs on an Au(111) surface, retracted the tip back, pulsed the potential of the substrate to generate H_2 at the particle which was collected amperometrically at the tip (SECM substrate generation, tip collection, SG/TC mode).[175] A similar approach made a topographical map of an Au electrode surface and the tip coordinates were retraced, but with a small offset distance from the surface (lift mode) whilst the substrate potential drove the reduction of $[Ru(NH_3)_6]^{3+}$, collected as $[Ru(NH_3)_6]^{2+}$ at the tip.[176] While both of these approaches acquired electrochemical information about the surfaces in question, they were limited by the probe electrode (tip). In the first case the tip was much larger than the Pd particle studied and in the second, the precise geometry of the nanoelectrode used was difficult to elucidate, hence effective modeling of the SECM data was not possible.

Recently, there has been renewed interest in the STM-SECM format, likely due to improvements in methods for the fabrication of nanoelectrodes (Section 2.3). A recent SECM based study of 14 nm Pd nanocubes (dispersed on a support) with a 10 nm Pt SECM tip showed spatial-resolution much higher than would have be expected (see above, Figure 1B-ii). Under further investigation it was suggested that the response was actually due to the electron tunneling between the nanocube and a very small, but sharp, point on the tip.[42] The same authors have performed subsequent studies, where they studied AuNPs (but supported on an insulating surface) with a tunneling mode of SECM. It was shown that when a Pt nanoelectrode tip was *ca.* > 4 nm from the AuNP surface, positive feedback was observed, as the redox probe used (FcMeOH), oxidized at the tip was recycled at the AuNP surface (*i.e.*, reduced at the AuNP). Upon closer approach however, electron tunneling occurs between the tip and AuNP,

resulting in the AuNP essentially acting as an extension of the nanoelectrode (tip) surface. This was reflected in steady-state voltammograms run in the SECM and tunneling regimes, where an increased steady-state current in $[Ru(NH_3)_6]^{3+}$ reduction (due to the increased area of NP versus the tip) and a delayed onset potential for the HER (in $HClO_4$) was observed in the tunneling regime (due to the difference in HER overpotential between Pt and Au).[177,178]

As discussed earlier (Section 2.3), robust fabrication procedures for nanoelectrodes are of critical importance to advance nanoscale SECM and STM-SECM. Recently, 100 nm Au nanoelectrodes, fabricated using the previously described Au bipolar electroless plating method, have demonstrated the ability of these nanoelectrodes to use the tunneling feedback to approach the surface for further SECM studies of an array of AuNPs.[74] A similar methodology was reported but for electrodes with a 30 nm diameter (Figure 2C); this dramatic decrease in size undoubtedly opens the door for further resolution increases in STM-SECM.[72]

6. Scanning Electrochemical Cell Microscopy (SECCM)

The final SEPM technique to be considered herein is SECCM. The instrumentation and working principles of SECCM have been described in detail in a number of previous reviews.[5,179,180] Here, we will summarize the basic operational principles of SECCM; give an overview of how the technique has evolved over time, including a look to the future with the current state-of-the-art in terms of image acquisition speed, resolution and multifunctionality; and discuss recent applications of this technique in the field of nanoelectrochemistry, particularly nanoscale electrochemical imaging.

6.1 Operational Principles

In SECCM, local electrochemical measurements are performed within a confined area of a surface, defined by the dimensions of the droplet (meniscus) formed at the end of a pulled glass capillary (*i.e.*, nanopipet, see Figure 9A) that is filled with electrolyte solution of interest. A QRCE is inserted into the back of the probe, and electrochemical (*e.g.*, voltammetric) measurements are performed by applying a potential between this QRCE and the substrate (working electrode) surface.[5,179,180] Ag/AgCl wires are the most commonly used QRCEs in SECCM (and SICM, see Section 3), as they possess a stable reference potential and are non-fouling on the several hours timescale.[181] Alternative QRCEs, such as Pd wires saturated with hydrogen (Pd-H_2) are also available,[182,183] in addition to conventional three-electrode formats that make use of separate auxiliary (counter) and reference electrodes.[184] The probe and/or

substrate (working electrode) surface are mounted on *xyz* piezoelectric positioners (Figure 9A-i), allowing local measurements to be performed in an automated fashion (Figure 9A-ii), building up synchronous topographical (through the recorded *z*-positions) and electrochemical "maps" of the substrate, for example, through a series of spatially-resolved voltammetric experiments (Figure 9A-iii). In this way, particular surface features can be targeted (*e.g.*, individual grains and GBs, see Figure 9A) and subsequently characterized with co-located spectroscopy/microscopy, allowing structure and activity to be resolved *directly* and *unambiguously*.[5,158,179,180]

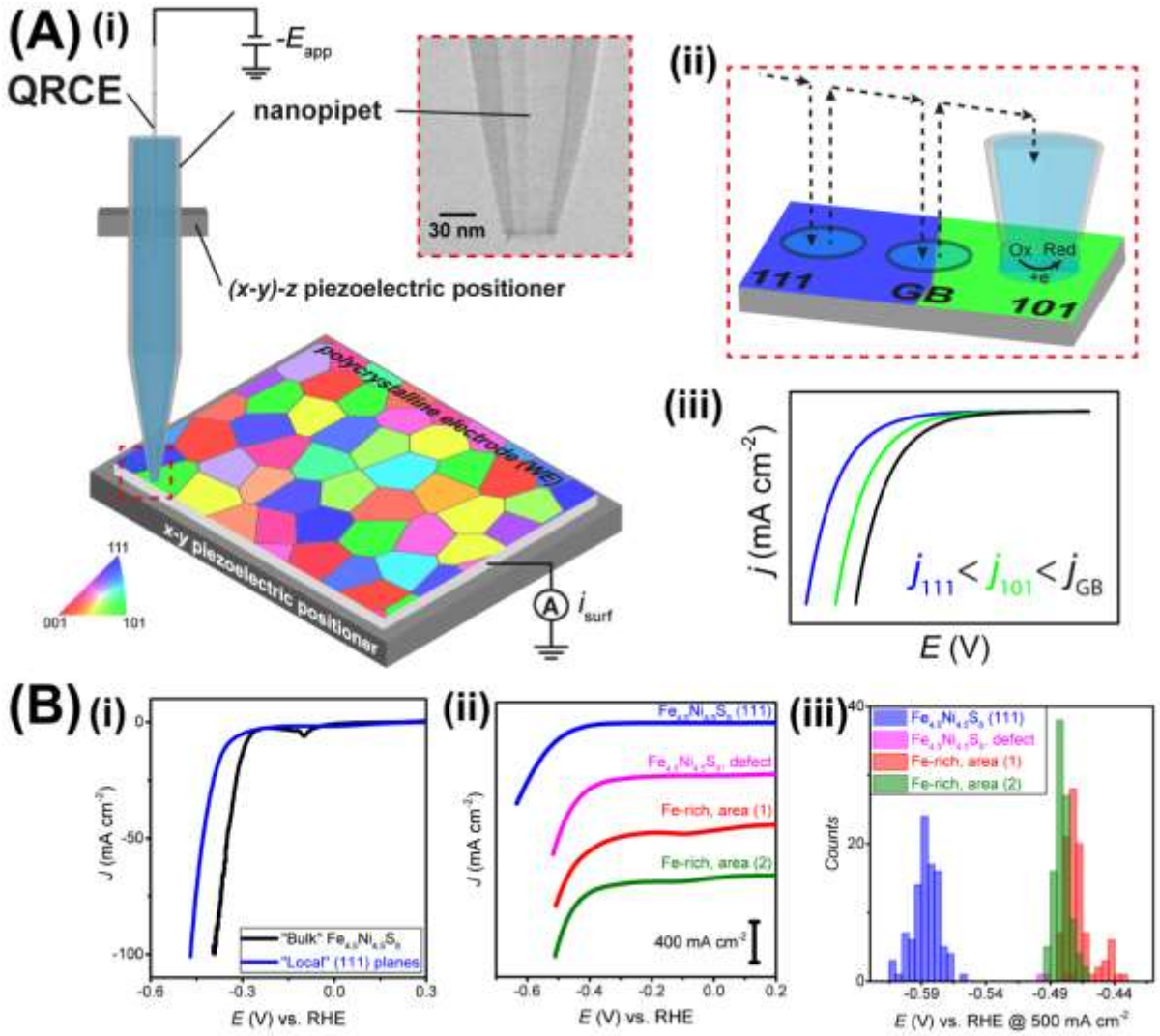

Figure 9. (A) Schematic showing the basic instrumental set up and operation of hopping mode SECCM. **(i)** SECCM configuration, with a single channel nanopipet probe (TEM image shown inset) mounted on (*x*-*y*)-*z* piezoelectric positioners, used to make local electrochemical (voltammetric) measurements at a model polycrystalline metal surface (also mounted on *x*-*y* piezoelectric positioners), by applying a potential (E_{app}) at the QRCE in the probe and

measuring the current at the surface (i_{surf}). **(ii)** Zoomed in view of the end (tip) of the probe during meniscus contact with the surface of interest (arrows indicate movement of the probe). **(iii)** Spatially-resolved linear sweep voltammograms (LSVs), simulating a surface-controlled (electrocatalytic) reaction at 3 sites on the model polycrystalline surface. **(B)** Exemplary spatially-resolved electrochemical data obtained in the SECCM format, from local voltammetric measurements of HER activity performed across the surface of iron nickel sulfides (nominally $Fe_{4.5}Ni_{4.5}S_8$) at pH = 1. **(i)** LSVs obtained at a nominally $Fe_{4.5}Ni_{4.5}S_8$ electrode in bulk solution (black trace) and locally at the (111) planes, using SECCM (blue trace). **(ii)** Representative LSVs and **(iii)** corresponding distribution (histogram) of potential required to achieve j = 500 mA cm^{-2}, obtained at different surface sites of $Fe_{4.5}Ni_{4.5}S_8$, including the (111) plane (blue trace), a macroscopic defect site (pink trace) and two Fe-rich areas (red and green traces). (B) was adapted from Local Surface Structure and Composition Control the Hydrogen Evolution Reaction on Iron Nickel Sulfides, Bentley, C. L.; Andronescu, C.; Smialkowski, M.; Kang, M.; Tarnev, T.; Marler, B.; Unwin, P. R.; Apfel, U. P.; Schuhmann, W., *Angew. Chem. Int. Ed.*, Vol. 57, Issue 15 (Ref 185). Copyright 2018 Wiley.

6.2 Development and State-of-the-Art

Microcapillary-based techniques, with probes on the 1 to 1000 µm scale, were first used over two decades ago to probe the local corrosion-related properties of macroscopic electrode (*e.g.*, polycrystalline metal) surfaces.[186,187] Drawing inspiration from this, the scanning micropipet contact method (SMCM) was developed, where a single channeled micropipet probe, mounted on *xyz* positioners, is used to make local electrochemical measurements in an automated fashion, as described above (*i.e.*, see Figure 9A).[188] This configuration uses the hopping mode (see also Section 3.1), where the probe is approached to the substrate (working) surface at a series of predefined locations and, upon each meniscus landing, an electrochemical (*e.g.*, voltammetric, *i-E* or chronoamperometric, *i-t*) experiment is carried out. During approach, when the meniscus protruding from the end of the micropipet initially makes contact with the substrate (note that in SMCM and SECCM, the probe itself never makes physical contact with the surface of interest), a two electrode electrochemical cell is formed, and the current that flows as a result (due to closing the electrochemical circuit) is used as feedback to halt the *z*-approach.[182,188-190]

One of the major advantages of SMCM (and SECCM, see below) over alternative SEPM methods (see above), is that the electrochemical properties of a surface are probed *directly* and *locally* with integrated probe positional feedback. This means that well-known

electrochemical techniques, such as cyclic voltammetry, can be applied directly, but in a format where the "active electrode area" (dictated by the area wetted by the meniscus cell) is on the (sub)microscale and mobile, enabling thousands of spatially-resolved measurements to be made across a surface, which can be subsequently analyzed quantitatively.[158,179,191] A pertinent example of this is shown in Figure 9B (discussed further below). As a good rule of thumb, the meniscus cell wets surfaces with a dimension similar to the end of the pipet, discussed extensively at the recent Electrochemistry at Nano-interfaces *Faraday Discussion*.[192] The small currents (typically 10s of pA) measured in SMCM (and SECCM) also render these techniques relatively immune to bulk sample resistance (*i.e.*, ohmic or *iR* drop, where *R* is resistance), which is a major problem for macroscopic measurements on resistive materials (such as molybdenum disulfide, see Section 6.3.2).[182,193] Finally, in SMCM (and SECCM) there is no need to fully immerse the substrate during measurement (as in macroscopic voltammetry or SECM), opening up the possibility of using materials that are usually difficult to encapsulate as an electrode, including layered or two-dimensional materials[193-195] and TEM grids.[196] Should materials be sensitive to the ambient environment, then environmental control,[197-199] and/or *in situ* electrochemical cleaning of the sample during the scanning process, can be implemented.[197]

Building on from the SMCM technique, dual-channeled theta pipet probes that are able to provide positional feedback independent of the current flowing at the substrate (working electrode) surface (as in SMCM) were later developed and the term SECCM was coined.[200] In this configuration, a potential bias is applied between QRCEs placed in the barrels of the theta pipet probe to induce an ion conductance current (as in SICM, see Section 3) across the meniscus. During operation, the probe is usually modulated (sinusoidal waveform) normal to the substrate surface, and once meniscus contact has been established, the ion conductance current will show a periodic modulation at the same frequency of the oscillation due to reversible deformation of the meniscus (droplet) cell. The ion conductance current, particularly the AC component, is very sensitive to the morphology of the meniscus cell (*i.e.*, it can indicate on wetting or spreading of the meniscus) and serves as an independent feedback signal to position the probe relative to the surface of interest.[179,191,200]

Ion conductance current feedback control afforded by the dual channel configuration of SECCM allows this technique to be operated in a constant distance scanning mode, where the position of the probe relative to the substrate surface (*i.e.*, meniscus height) can be readily controlled and maintained in three dimensional space, independent of substrate conductivity or

reactivity, allowing SECCM to probe a variety of substrate materials, including insulators[201,202] and semiconductors,[195,203] as well as opening up possibilities in nanoscale fabrication[204] and patterning.[205] High-speed, high-resolution approaches have also been developed for the constant tip-substrate scanning mode of SECCM, using an Archimedes spiral-scanning pattern (also employed in SICM reaction mapping[118], see Section 3.3.2) to obtain potential-resolved image sequences comprising thousands of pixels at rates as fast as *ca.* 4 seconds per frame (where each potential is a single frame).[206] In addition, SECCM has been combined with other SEPM methods, such as SECM, through the use of multi-functional quad-channel probes, where two-channels are equipped with QRCEs and filled with electrolyte (as in SECCM), while the other two serve as independent microelectrodes (as in SECM), enabling localized high-resolution amperometric imaging with integrated positional feedback.[71]

Most recent SECCM studies have re-adopted the hopping mode approach of SMCM (see Figure 9A) to perform spatially-resolved voltammetric analysis on a series of targeted surface features (Figure 9B). In addition to being readily interpreted through classical electrochemical methodology, spatially-resolved voltammetric current-potential (*i*-*E*) data can be combined to create dynamic electrochemical flux movies over a wide potential range (*i.e.*, range of current densities, *j*) with nanoscale resolution.[207] In addition, re-introduction of the hopping mode has re-enabled the use of single-channeled probes and simplified experimental set ups, with great advances in terms of spatial-resolution and image acquisition rates being recently reported in the field of nanoscale electrochemical imaging.[182,189,190] The current state-of-the-art, in terms of imaging resolution and speed, was recently achieved with a fine probe of tip diameter ≈ 30 nm (see Figure 9A-i), which was used to construct synchronous topographical and electrochemical maps comprised of thousands of pixels, where surface features as small as *ca.* 3 nm in height were resolved (few layer step edge on MoS_2, see Section 6.3.2) at acquisition rates as fast as 1.65 seconds per image (potential) frame.[182,190] There is scope to improve this resolution further, with sub-10 nm pipet probes previously being reported, but have never been used for imaging of any kind.[208] Filling such fine pipets may be difficult using the conventional "back-filling" approach, necessitating the adoption of novel filling protocols such as the recently reported "microdistillation technique".[209] Note, that for brevity, all meniscus cell-based techniques regardless of whether single or double channeled probes were used, are collectively referred to as SECCM henceforth.

6.3 Applications in Nanoscale Electrochemical Mapping

6.3.1 Carbon Materials. Well-defined sp^2 carbon materials, characterized by long-range order (graphene, graphite and carbon nanotubes) are widely used and studied materials in all fields of electrochemistry, including sensing, electrocatalysis and energy storage.[158] In addition to the predominant basal surface (or side wall for nanotubes) that make up these materials, there are a variety of defects, with the source and/or method of synthesis dictating the type, concentration and distribution of these localized surface sites. Despite the longstanding view, derived from classical "bulk" electrochemistry, that these defect sites dominate the macroscopic electrochemical activity of sp^2 carbon materials, studies carried out with electrochemical imaging techniques, most notably SECCM, in conjunction with co-located structural characterization (notably Raman microscopy) have highlighted the high activity of the basal surface (or side walls of nanotubes) for both simple redox reactions, as well as certain coupled electron–proton transfer processes.[194,195,203,210] Here we limit our focus to SECCM studies carried out on sp^2 carbon that were not covered in a recent comprehensive review on this topic,[158] as well as recent studies on boron doped diamond (BDD), a "designer" sp^3 carbon material that is finding a multitude of electrochemical applications.[211]

Local voltammetric (*i*-*E*) measurements with SECCM have been used to map the spatially heterogeneous activity of blistered graphite electrodes towards the catalytic oxidation of hydrazinium ($[N_2H_5]^+$ at pH = 7.4). The blistered surface of HOPG, induced by anion intercalation at highly oxidizing potentials (see Section 4.2), was shown to be rich in oxygenated defects (*e.g.*, graphite/graphene oxide moieties, mapped by micro-Raman spectroscopy), which has a dramatic effect on the $[N_2H_5]^+$ oxidation kinetics. Significantly enhanced electrocatalytic activity was measured at the defective blistered surface, evidenced by a significant cathodic shift (*ca.* 0.8 V) in the onset potential, as well as lower Tafel slopes (100 – 180 mV/decade versus 250 – 400 mV/decade) compared to the unmodified basal plane. Several factors were proposed to explain the dramatic effect of HOPG blistering on $[N_2H_5]^+$ electro-oxidation, including enhanced adsorption at negatively charged defect sites, enhanced ion-solvent (de)intercalation during electrocatalysis and/or reduced susceptibility to N_2 nanobubbles (produced as a result of the reaction) blocking surface access.[183]

SECCM has also been used to rationalize the macroscopic (bulk) electrochemical response of HOPG and oxygen terminated polycrystalline BDD (O-pBDD) towards the oxidation of dihydronicotinamide adenine dinucleotide (NADH). Bulk voltammetry at HOPG was relatively invariant with respect to step edge density (tested with different grades of

HOPG), suggesting that the basal plane is largely responsible for the macroscopic electrochemical response, which degraded rapidly with potential cycling due to fouling by reaction products. This observation was confirmed by nanoscale SECCM measurements, where the basal surface exhibited significant activity towards NADH oxidation, with no obvious enhancement at step edges. Macroscopic measurements at O-pBDD revealed that while it is less active than HOPG, it is also less susceptible (but not immune) to surface fouling, while microscopic voltammetric measurements (with SECCM) revealed a strong grain dependence, with activity scaling with local (grain-dependent) dopant density.[212]

Local electrochemical measurements with SECCM can be coupled with co-located *ex situ* electron back scatter diffraction (EBSD) characterization to resolve structure-activity at the individual grains and GBs that comprise a polycrystalline surface.[184,213] This "pseudo single-crystal approach" was employed to understand the microscopic factors (surface termination and doping level) determining the electrochemical solvent window (*i.e.*, the potential range over which the solvent/electrolyte is stable to electrolysis) of O-pBDD and hydrogen- terminated polycrystalline BDD (H-pBDD) in aqueous potassium chloride. Only grains of the (110) orientation with different boron-doping levels (revealed by micro-Raman mapping) were considered in order to rule out crystallographic effects on solvent/electrolyte breakdown kinetics. It was shown that doping level has a significant influence on solvent/electrolyte hydrolysis, with lower dopant levels leading to wider solvent windows (*e.g.*, 450 mV wider in the case of O-pBDD), indicating that the higher doped grains are more (electro)catalytic. Surface termination was found to have a much more dramatic influence on solvent window, with H-pBDD having a >1 V wider window than O-pBDD (1.25 and 1.17 V on less and more doped grains, respectively), which was attributed to differences in the HER kinetics on the cathodic side and different solvent/electrolyte breakdown reactions on the anodic side (*i.e.*, Cl^- oxidation is facilitated at O-pBDD, but not H-pBDD).[214]

6.3.2 Electrocatalytic Materials. SECCM has shown great promise as a screening tool in the field of electrocatalysis, where local electrochemical measurements, coupled with co-located structural analysis, can *directly* and *unambiguously* reveal the reactive sites that govern macroscopic reactivity, a crucial step in the rational design of functional materials with enhanced activity and/or stability.[215] This was clearly demonstrated in a recent study on nominally single-crystal iron nickel sulfides (nominally $Fe_{4.5}Ni_{4.5}S_8$), which are highly efficient HER electrocatalysts in bulk form. Local voltammetric (*i*-*E*) measurements carried out using SECCM revealed apparently "lower" activity from the (111) planes of $Fe_{4.5}Ni_{4.5}S_8$ (reflecting

the intrinsic activity of the basal surface) compared to the macroscopic (bulk) activity, as demonstrated in Figure 9B-i. This observation suggests that local heterogeneities, such as defects (or compositional differences), which would be exposed to solution in the bulk measurements but necessarily not the local ones, are largely responsible for the observed macroscopic activity. Indeed, this was directly confirmed by performing local measurements on a macroscopic "defect" site on the $Fe_{4.5}Ni_{4.5}S_8$ basal surface, which gave rise higher current densities (*i.e.*, higher activity) at a given overpotential (η), as shown in Figure 9B-ii. It was also found that local composition can play an important role, with Fe-rich material, which possessed segregated regions with higher Fe:Ni ratios compared to nominal 1:1 (as in $Fe_{4.5}Ni_{4.5}S_8$), exhibiting higher activity, as shown in Figure 9B-ii and iii.[185] It is worth noting that as the SECCM droplet cell configuration (see Figure 9A) mimics the three-phase boundary operating in low temperature fuel cells, the complications normally associated with gas bubble formation (*e.g.*, H_2 in the case of the HER) at high catalytic current densities (*e.g.*, 500 mA cm^{-2} in Figure 9B-iii) are not encountered.[185,193]

SECCM has also been employed to perform local voltammetric (catalytic) measurements on natural (single-crystal) molybdenite (MoS_2), a layered material that has received considerable attention as an earth-abundant HER electrocatalyst.[215,216] Correlation between local electrochemical and co-located topographical information (from AFM[193] or collected synchronously with a fine probe of tip diameter ≈ 30 nm,[182] see Figure 10A-i) revealed uniform HER activity on the basal plane at the μm length-scale and elevated currents (*i.e.*, enhanced activity) at the edge plane (see Figure 10A-ii), which scales with the number of exposed MoS_2 layers (*i.e.*, step height, see Figure 10A-iii),[182,193] in line with macroscopic electrochemical studies on ensembles of exfoliated/synthesized material and theoretical predictions.[216,217] Furthermore, semi-quantitative Tafel analysis demonstrated that the so-called "catalytically inert" basal surface (expected to contain some point defects, such as sulfur vacancies) possesses an exchange current density (j_0) comparable to moderate HER catalysts such as Au and Cu, while the edge plane possesses a j_0 value that is estimated to be >10 times larger.[193]

Fine nanopipet probes (tip diameter ≈ 30 nm, see Figure 9A) have also been used to elucidate the spatially-resolved *i-E* behavior of individual nano-entities supported on glassy carbon (GC), such as triangular/hexagonal (111)-oriented Au nanoplates[190] (Figure 10B) and electro-deposited non-faceted polycrystalline AuNPs,[182] (Figure 10C). Considering only the *i-E* measurements taken on top of the Au nanoplates (slight droplet cell spreading or instability

is observed around particle edges),[182] uniform activity was observed at both the inter- and intra-particle level upon cathodic polarization in aerated acidic media (*i.e.*, processes under investigation are ORR and HER), as expected from a well-defined single-crystalline material. This can be clearly seen by comparing the high-resolution topographical and electrochemical maps in Figure 10B-i and ii, respectively, where uniform currents of *ca.* –12 pA are measured on top of each of the individual nanoplates (representative scanning electron microscopy, SEM images shown in Figure 10B-iii), which contrasts the uniformly inactive GC support (*i.e.*, blue areas in Figure 10B-ii).[190] By comparison, while the non-faceted polycrystalline AuNPs exhibited relatively uniform activity towards catalytic $[N_2H_5]^+$ oxidation at the inter-particle level (*i.e.*, average taken across the top surface of individual AuNPs), reaction rates varied significantly at the intra-particle level (*i.e.*, across the surface of a single AuNP), indicating that these single entities (AuNPs) are not uniformly active. The spatial variation in catalytic activity was attributed to structural (crystallographic) heterogeneities and can be clearly seen by comparing the topographical and electrochemical maps in Figure 10C-i and ii, respectively, where the current varies significantly from pixel-to-pixel, evident from the pixel-resolved *i*-*E* data in Figure 10C-iii.[182]

As noted above, in "pseudo single-crystal" SECCM, the individual grains and GBs that comprise a polycrystalline surface are independently interrogated, an approach that was recently used to rationalize the macroscopic response of polycrystalline Au for electrochemical CO_2 reduction (ECR). Bulk electrolysis, coupled with on-line product analysis, revealed increased selectivity for CO production relative to H_2 with increasing GB density, suggesting that GBs are more active than the grains for ECR, but not the competing HER. Local *i*-*t* measurements with SECCM confirmed this hypothesis, where line scans revealed elevated currents (*i.e.*, enhanced activity) at GB surface terminations under a CO_2 atmosphere, where both the ECR plus competing HER are possible, but not under an Ar atmosphere, where only the HER is possible. The width of the region exhibiting enhanced activity (*i.e.*, the "catalytic footprint") and degree of activity enhancement was shown to be dependent on the GB geometry, and from this it was postulated that GBs comprise strained or high-energy surfaces, that are highly active and (kinetically) stable under catalytic turnover conditions. On this basis, annealed (polycrystalline) Au foils were mechanically treated to artificially increase GB density, which translated into substantially increased ECR activity at the macroscale.[184] Again, it is worth noting due to the three-phase boundary configuration of SECCM, there is an

enhanced flux of gaseous species (*e.g.*, CO_2[182,184] or O_2[184,196]) across the meniscus (droplet) cell enabling high rates of mass-transport in this configuration.[197]

The droplet cell configuration of SECCM (see Figure 9A) can be used to encapsulate single or small populations of supported NPs, allowing for the high throughput screening of nanomaterials used in electrocatalysis or electrochemical energy storage (Section 6.3.3). For example, micron-sized probes were used to screen the electrocatalytic properties of α-phase and β-phase $Ni(OH)_2$ NPs of *ca.* 10 nm diameter (characterized *ex situ* TEM analysis), (electro)deposited directly on single-walled carbon nanotubes (CNTs), supported on insulating Si/SiO_2. The CNT-supported disordered α-phase $Ni(OH)_2$ NPs were shown to exhibit specific activities towards alcohol (methanol or ethanol) oxidation that are *ca.* 1 order-of-magnitude greater than the ordered β-phase. The remarkable alcohol oxidation activity of the α-phase $Ni(OH)_2$ NPs was attributed to the disordered structure enabling more ready ion-solvent (de)intercalation during electrocatalysis, as well as the high oxidation state of γ-NiOOH [+3.5, formed from α-$Ni(OH)_2$] compared to β-NiOOH [+3.0, formed from β-$Ni(OH)_2$], which are the species responsible for alcohol oxidation catalysis.[218]

The SECCM droplet cell configuration was recently used to probe the ORR response of a small population ($N < 16000$) of size-selected Pt nanoclusters (PtNCs, 923±27 atoms in each cluster, deposited with a cluster beam source) deposited onto a carbon-coated TEM grid support. PtNC deactivation was found to be strongly surface coverage dependent, with activity decreasing significantly at low surface coverage (*ca.* 6%) during electrochemical (voltammetric) cycling, but staying relatively constant at high surface coverage (*ca.* 37%). Supported by *ex situ* x-ray photoelectron spectroscopy measurements, this phenomenon was postulated to be due to poisoning of the PtNCs by carbon- and oxygen-containing moieties that are produced by the reaction of reactive oxygen intermediates (generated transiently in the ORR), with the carbon support (*i.e.*, carbon corrosion), which becomes less likely at high surface coverage, where the distance between neighboring PtNCs is small. The deposition impact energy was also shown to affect cluster stability drastically during electrochemical cycling, with PtNCs deposited with low impact energy migrating as a result of the ORR, explained with the support of FEM modeling to be due to electrochemical propulsion caused by an uneven flux distribution around individual PtNCs within the ensemble.[196] The use of a TEM grid as a substrate for both electrochemistry with SECCM[219] and high-resolution structure measurements with TEM techniques should be of huge benefit in the future for screening and discovering optimal electrocatalysts.

A very recent study coupled SECCM with *in situ* optical hyperspectral imaging to directly study the catalytic oxidation of hydrazine at individual Au nanorods, supported on indium tin oxide (ITO). This approach, coined optically targeted electrochemical cell microscopy (OTECCM), enables individual nanostructures to be located and structurally characterized (*i.e.*, composition, size and/or geometry) *in situ*, allowing SECCM to be carried out in a targeted fashion, rather than the usual scanning mode (*i.e.*, hopping mode). A diversity of electrochemical (*i*-*E*) responses were measured among Au nanorods of comparable size, with some activating with successive cycling, while others deactivated. *In situ* spectroscopic investigation indicated that the gross geometry of the individual nanorods (*i.e.*, size or aspect ratio) is a poor predictor of catalytic activity, suggesting that variation in sub-nm structural features (defects) and/or ligand coverage play a dominant role.[220] In the future, we expect further applications that combine SECCM or other SEPMs with micro-spectroscopy.

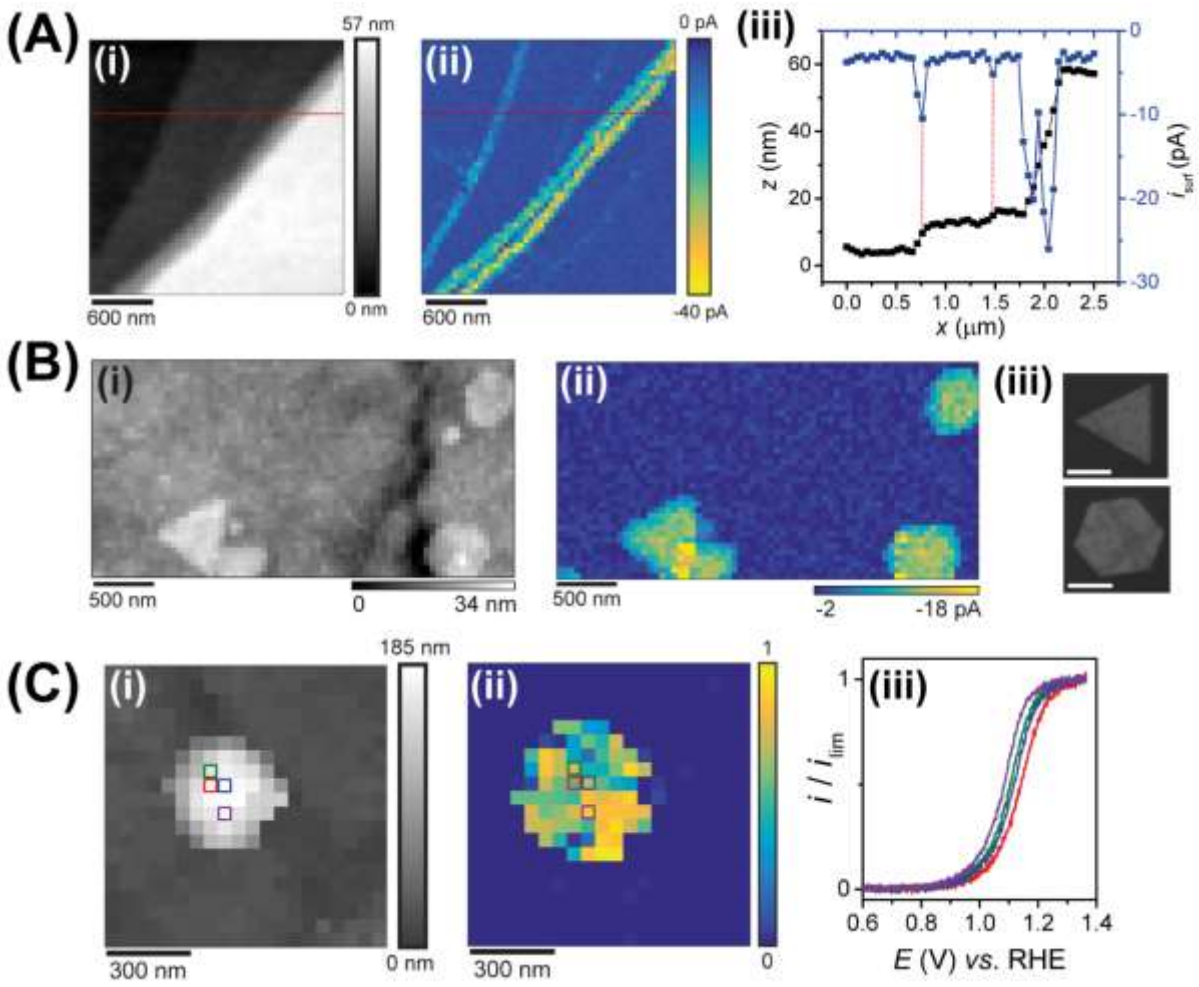

Figure 10. (A) Synchronous **(i)** topographical and **(ii)** electrochemical (E = –0.857 V vs. RHE) maps, visualizing HER activity on the cleaved surface of MoS_2 (natural crystal) at pH = 1. **(iii)**

Line scan profiles of *z*-height (black trace) and i_{surf} (blue trace) taken across the surface of MoS_2, indicated by the dashed red lines in (i) and (ii). **(B)** Synchronous **(i)** topographical and **(ii)** electrochemical maps (E = –0.43 V vs. RHE), visualizing the uniform ORR/HER activity of GC-supported Au nanoplates at pH = 1. **(iii)** Representative FE-SEM image of the triangular and hexagonal (111)-oriented Au nanoplates (scale bar indicates 500 nm). **(C)** Synchronous **(i)** topographical and **(ii)** electrochemical maps (E = 1.15 V vs. RHE), visualizing the electrocatalytic oxidation of $[N_2H_5]^+$ on the surface of a GC-supported AuNP at pH = 1. **(iii)** Normalized LSVs collected at the individual pixels labelled in (i), demonstrating the non-uniform activity measured across the surface of AuNPs. All topographical/electrochemical maps in (A-C) were obtained in the voltammetric hopping mode SECCM configuration (each pixel is an individual LSV experiment, see Figure 9A), with probe of tip diameter ≈ 30 nm. (A) and (C) were adapted from Bentley, C. L.; Kang, M.; Unwin, P. R. *J. Am. Chem. Soc.* 2017, 139, 16813-16821 (Ref 182). Copyright 2017 American Chemical Society. (B) was adapted from Bentley, C. L.; Unwin, P. R. *Faraday Discuss.* 2018, 210, 365-379 (Ref 190) with permission from the Royal Society of Chemistry.

6.3.3 Energy Storage Materials. Analogous to the electrocatalysis examples above, SECCM has recently been adapted as a tool for screening the electrochemical (charge/discharge) characteristics of energy storage (battery) materials. For example, the SECCM configuration has recently been used to encapsulate and electrochemically characterize (galvanostatic[198] or cyclic voltammetric waveforms[198,221]) small populations of $LiFePO_4$ particles within an ensemble. Less than 10 particles (*ca.* 100 nm in diameter) were probed in each experiment, and the micropipet probe was filled with either propylene carbonate (containing 5 mM $LiClO_4$)[198] or the ionic liquid, 1-ethyl-3-methylimidazolium bis(trifluoromethanesulfonyl)imide,[221] under a controlled (Ar) atmosphere. Higher rates of galvanostatic charge/discharge could be achieved in the SECCM format compared to bulk, attributed to significant mass-transport limitations and ohmic effects in the latter "composite electrode" configuration.[198] Cyclic voltammetry revealed significant variations between the electrochemical performance of different particles (or collection of particles) within the ensemble, evidenced by differences in the cyclic voltammetric peak morphologies (single *vs.* double peak) and potentials, attributed to particle-to-particle variations in particle-support contact, structural factors (*i.e.*, particle geometry or defects in lattice structure) and/or chemical impurities.[198,221]

In the study above, it was noted that the electrolyte based on propylene carbon undergoes significant wetting (*ca.* 10 μm area from a probe of $d_t \approx 1$ μm) on the substrate

surface.[198] Thus, in order to overcome the wetting issue normally associated with organic-based electrolytes, a gel-polymer electrolyte based on low molecular weight poly(glycidyl methacrylate) and dimethylsulfoxide was used to probe the electroactivity of the conformal layer (*i.e.*, the structure that is normally formed at the cathode during discharge in lithium-air batteries) versus toroidal Li_2O_2 in a controlled atmosphere (Ar). Spatially-resolved cyclic voltammograms revealed greatly enhanced electroactivity at the toroidal Li_2O_2 particles (*ca.* 1 to 1.5 μm in diameter, located *in situ* from topographical data) with *ca.* 9 times higher voltammetric peak currents for the oxidation process, and a *ca.* –500 mV shift in onset potential compared to the insulating conformal layer.[199]

6.3.4 Fabrication. For completeness, it should be noted that in addition to electrochemical imaging, significant progress has recently been made in the use of the SECCM meniscus "nanocell configuration" for surface patterning and controllable fabrication of three dimensional (nano)structures. Recent examples in this area include surface patterning of electrodes with polyacrylamide gel,[222] micropatterning of surfaces with reduced graphene oxide microwires by "meniscus-guided printing",[223] "meniscus-on-demand" nanoprinting of freestanding nanowire arrays with multi-channel nanopipets,[224] fabrication of "soft polypyrrole microcontainers" through microbubble-assisted templating[225] and *in situ* fabrication of nanopore arrays for single-molecule sensing, induced by dielectric (SiN) breakdown through meniscus contact.[226] SECCM and other meniscus probe formats are very well suited to micropatterning and nanopatterning and we envisage further applications in the future.

7. Nanoscale Electrochemical Mapping with Optical Techniques

Optical super-resolution microscopy methods are emerging as powerful tools for visualizing nanoscale electrochemistry[227] that complement SEPM methods and may find increasing combination with them in the future. Fluorescence-based techniques, in particular, could offer the ultimate sensitivity for the analysis of electrochemical interfaces through single molecule detection.

In a recent study, *in situ* fluorescence microscopy was used to visualize single catalytic turnover events on individual 50 nm PtNPs in a nanoconfined environment (*i.e.*, sandwiched between an optically transparent solid 100 nm SiO_2 core and a mesoporous SiO_2 shell, with aligned nanopores of *ca.* 2.3 nm in diameter).[228] The non-fluorescent reactant, amplex red was oxidized by hydrogen peroxide at the surface of the PtNPs to generate highly fluorescent resorufin molecules. This approach allowed the heterogeneous molecular transport and

catalytic reaction kinetics within nanopores to be quantified with single-molecule and single-particle resolution, demonstrating a significant increase in reaction rate in the presence of nanoconfinement.[228] A similar approach was applied to unravel the cooperative communication within and between single Pd- and Au-based nanocatalysts.[229] Surface "active" sites on single Pd or Au nanocatalysts were shown to communicate with each other (*i.e.*, intra-particle level) during heterogeneous catalysis over a distance of *ca.* 10^2 nm, with a temporal memory of 10^1 to 10^2 seconds. Inter-particle communication was also identified, to relate reactions on different nanocatalysts spatiotemporally over a distance on the μm scale.[229]

Adsorption, desorption, and heterogeneous redox events of individual resorufin molecules were investigated on ITO electrodes modified with mesoporous silica using total-internal reflection fluorescence microscopy.[230] The 0.7 zL silica channels (3 nm diameter and 100 nm long) reduced the rate of diffusion of fluorogenic redox molecules, enabling real-time imaging of single-molecule redox events. Coupled with a 2-electrode electrochemical set-up, the measurement of the potential-dependent surface population of resorufin molecules confirmed that the oxidation of this redox mediator is an adsorption-controlled electrochemical process.

Super-resolution fluorescence microscopy can also be applied to follow dynamic processes of NP collision and oxidation in a one-dimensional space. For example, in a recent study,[76] an innovative nanochannel cell configuration was developed to optically monitor the dynamic collision and oxidation of AgNPs *in situ* using single-particle fluorescence microscopy. The nanochannel cell was fabricated by depositing a PtNP at the orifice of a nanopipet, which functions as a nanoelectrode in the bipolar regime when immersed in an acidic aqueous solution. In this configuration, AgNP motion and stripping was found to be sluggish (*ca.* 1000 times slower) compared to bulk solution, attributed to hindered mass-transport and electrostatic effects in the nanochannel cell. AgNPs were observed to move in and out of contact with the Pt nanoelectrode during oxidation (*i.e.*, repeated collisions), which was postulated to be modulated by strong electrostatic attraction (unbiased AgNPs are negatively charged and the biased electrode is positively charged) and repulsion (biased AgNPs and electrode are positively charged) at the electrode/solution interface.[76]

Imaging of nanobubble nucleation and growth is another example of the application of super-resolution fluorescence microscopy. Labeled with the Rhodamine 6G fluorophore, nanobubble formation in electrochemical water splitting was followed on ITO electrodes.[231]

On bare ITO electrodes, the authors claimed to observe the formation of hydrogen nanobubbles even at early stages in water electrolysis, *i.e.*, > 500 mV before reaching the thermodynamic reduction potential. On ITO electrodes decorated with Au nanoplates, nanobubble nucleation frequency was observed to be generally higher on and within a 3 μm radius of the active nanoplates, which was attributed to the "hydrogen spillover effect".

Super-resolution imaging can also be a complementary tool to the nanopipet based approaches discussed in detail above. For instance, a nanopipet (in the SICM configuration, see Section 3) was used for targeted delivery of fluorescent polystyrene NPs (radius = 130 nm) on the transparent ITO surface.[232] Coupled to this device, a 3-D super-resolution fluorescence microscope was employed to resolve positional information on the fluorescent NPs with the precision of 10s of nanometers. In the absence of the pressure driven flow, the NPs experienced (potential-dependent) attractive forces at an electrified interface, resulting in hindered (subdiffusive) transport. However, under the pressure driven flow, superdiffusion was observed indicating the competition between the force originating from fluid and the electric field. This provided an effective strategy for manipulating the NPs trajectories in real time.

Plasmonic based tools are another growing branch among nanoscale optical imaging techniques, highlighted in several recent reviews.[7,8] An approach of this type was recently used to study surface electrochemical processes (*i.e.*, surface oxide/stripping in alkaline media) on individual gold nanowires (1 to 10 μm in length) within an ensemble of such nanowires. The cyclic voltammograms measured at individual nanowires were different from those for bulk Au, featuring sharper oxidation (oxide formation) peaks and reduction (oxide stripping) peaks that occurred at more negative potentials. In addition, heterogeneity in the morphology (*i.e.*, size, shape and position) of the oxidation/reduction peaks was observed between individual nanowires in the ensemble (inter-particle level), as well as along a single nanowire (intra-particle level, *ca.* 500 nm resolution), with currents not simply scaling with nanowire size (smaller nanowires of less than 1 μm were more active overall).[233] A similar set-up was also employed to "image" the electrochemical current associated with single $LiCoO_2$ NPs during cyclic voltammetry and charge/discharge.[234]

Recent advances have led to the coupling of plasmonic imaging with electrochemical impedance spectroscopy (EIS), combining advantages of these techniques.[235] In this approach, an EIS spectrum is generated optically, by converting the local surface charge associated with the modulated current into a plasmonic signal. An electric field can be generated locally by

positioning a pipet over a substrate electrode to be investigated and applying potential between a QRCE in the nanopipet and the substrate.[236] For example, a *ca.* 700 nm diameter pipet was used to scan the local EIS response from an Au substrate, enabling determination of the surface charge and the local electric field at the electrode surface.[236] This study opens up prospects for coupling SICM with plasmonic-based imaging.

It is interesting to compare the relative merits of SEPM methods, which have been of most interest in this article, and optical methods. The optical methods we have briefly reviewed, while extremely powerful and ultrasensitive, are limited to the use of certain materials (*i.e.*, optically transparent supports and plasmonic materials in surface plasmonic resonance) and/or probe molecules (*i.e.*, redox fluorophores in super-resolution fluorescence). In contrast, the SEPM techniques can be applied more generally to broader classes of electrochemical processes. The physical origin of the measured signal is obviously another major difference between SEPMs and optical methods. SEPM signals are the integral response of many electrochemical events, while certain optical methods are able to register single molecule reactions ("events"). Therefore, the two classes of technique provide complementary information, making them very valuable in the toolbox of nanoscale electrochemical mapping, as evident from the recent examples mentioned above. In the future, the combination of SEPMs and optical techniques could prove to be a very powerful route for visualizing dynamics at electrochemical interfaces.

8. Other Electrochemical and Electronic Imaging Techniques

There are a variety of other local electrochemical methods, including scanning kelvin probe, adapted to map the electrode potential under thin electrolyte layers and at hindered interfaces,[237-239] scanning vibrating electrode technique, capable of mapping local ionic currents in the vicinity of electrochemical interfaces,[240,241] the scanning ion selective electrode technique, designed to define local concentrations (*i.e.*, ion flux gradients),[242,243] and local electrochemical impedance spectroscopies,[244,245] allowing the study of the kinetics of heterogeneous electron-transfer and the properties of double layer or adsorption processes. In principle, all of these techniques could attain nanoscale resolution, however, in practice, they have thus far often been restricted to the microscale, owing to difficulties in scaling the probe size down, as well the working distance while immersed in an (electrolyte) solution. Again,

some of the innovations that we have reported in SICM and hybrid techniques could be an effective route to translate these techniques to the nanoscale.

9. Conclusions

This article has sought to capture recent innovations that have led to an inflection point in experimental capability for nanoscale electrochemical mapping. As pointed out in a recent perspective,[25] truly nanoscale SEPM is now established and is set to become more or less routine on the future. While presently based on a relatively small number of research groups, there is growing interest in nanoscale SEPMs as the methods become easier to implement using nanopipet-based probes, especially on SICM and SECCM platforms. These instrumental developments are very timely because of the considerable prominence of materials electrochemistry, on the one hand, and the growing need to gain better physicochemical descriptors of processes at single biological cells, on the other. SEPMs are ideally suited for many types of investigations in these broad areas.

In combination with complementary data from co-located microscopy and micro-spectroscopy techniques, nanoscale SEPMs offer unprecedented opportunity for determining structure-function-activity relationships at the nanoscale and determining the nature of active sites directly. From the examples presented in this article, we have shown how correlative electrochemical microscopy reveals active sites on electrodes and in electroactive materials unambiguously. There is thus huge potential for using nanoscale SEPMs to screen electroactive materials, deepen understanding of electrocatalytic materials and facilitate rational catalyst discovery and design.

Likewise, SEPMs are proving to be increasingly powerful in the life sciences, for visualizing surface charge, cellular flux processes, perturbing cellular environments and examining the consequences, and sampling and analyzing the intra-cell space. In particular, as we have shown in this article, there has been a coming together of the principles and methods of SICM and SECM, which operate with essentially the same equipment, to produce new techniques and instrumental understanding that have greatly expanded the range of phenomena that can be studied. The improved descriptions of nanoscale mass-transport in nanopipet systems in recent years, from FEM modeling, has enabled the design of new experiments and the quantitative analysis of data. Operating at the nanoscale means that authentic

representations of SEPM tips can be implemented to produce increasingly robust and realistic FEM models.

We have touched briefly on other methods for electrochemical mapping. Optical techniques are finding increasing application in quantifying single catalytic turnover events on nanostructured materials, as well as related processes such as adsorption, desorption and heterogeneous redox events, nucleation and growth of nanobubbles, tracking particle motion in single particle delivery and other related fields. Since SEPMs and optical methods provide complementary information, in the future their combination could prove to be very powerful for visualizing dynamics at electrochemical interfaces and in interfacial science generally.

List of Abbreviations

Abbreviation	**Meaning**
AC	alternating current
AFM	atomic force microscopy
BDD	boron doped diamond
CNT	carbon nanotube
DC	direct current
EBSD	electron back-scatter diffraction
ECR	electrochemical CO_2 reduction
EC-STM	electrochemical scanning tunneling microscopy
EIS	electrochemical impedance spectroscopy
FEM	finite element method
FIB	focused ion beam
GB	grain boundary
GC	glassy carbon
H-pBDD	hydrogen terminated polycrystalline boron doped diamond
HER	hydrogen evolution reaction
HOPG	highly oriented pyrolytic graphite
ITO	indium tin oxide
LSV	linear sweep voltammogram
NC	nanocluster
NP	nanoparticle
O-pBDD	oxygen terminated polycrystalline boron doped diamond
ORR	oxygen reduction reaction
QRCE	quasi-reference counter electrode
RHE	reversible hydrogen electrode
SECCM	scanning electrochemical cell microscopy
SECM	scanning electrochemical microscopy

SEM	scanning electron microscopy
SEPM	scanning electrochemical probe microscopy
SICM	scanning ion conductance microscopy
SMCM	scanning micropipet contact method
STM	scanning tunneling microscopy
TEM	transmission electron microscopy
UHV	ultra-high vacuum
UME	ultramicroelectrode

Biographies

Cameron L. Bentley is presently a Ramsay Memorial Fellow at the University of Warwick (UK). He was awarded his Ph.D. degree at Monash University (Australia) in 2015. He joined the Warwick Electrochemistry and Interfaces Group (WEIG) in 2016, initially supported by an Endeavour Research Fellowship (Australian Research Council) and later a Marie Skłodowska-Curie Individual Fellowship (European Commission). His current research focuses on applying scanning electrochemical probe microscopy to resolve nanoscale structure and activity in functional (electro)materials.

James Edmondson is a Ph.D. student at the Molecular Analytical Science Centre for Doctoral Training (MAS CDT), University of Warwick (UK). He holds an MPhys degree in Physics (2015) and MSc in Molecular Analytical Science (2016) from the University of Warwick. His current research involves the development and application of nanoscale electrochemical imaging techniques, specifically scanning tunneling microscopy and scanning electrochemical microscopy for nanoscale electrochemical studies of surfaces.

Gabriel N. Meloni is currently a Marie Skłodowska-Curie Research Fellow at the University of Warwick (UK) with WEIG. He has a B.Sc. (2012) and a Ph.D. (2017) degree in Chemistry, both from the University of São Paulo, USP (Brazil). He has been working on SEPM techniques since 2009, when he was a visiting student at the University of Venice under the tutoring of Prof. Salvatore Daniele. He spent 1 year as a visiting Ph.D. student (2015/16) at the University of Warwick, with Prof. Pat Unwin, working on multifunctional electrochemical probes for hybridizing SEPM techniques. He is currently working on the development of new electrochemical imaging techniques for investigating cellular process with subcellular resolution.

David Perry is a Leverhulme Trust Research Fellow in WEIG. He has a MMath. (2012) in Mathematics and a Ph.D. (2016) in Mathematical Biology and Biophysical Chemistry, under the supervision of Profs. Pat Unwin and Bruno Frenguelli, from the University of Warwick (UK). David spent his Ph.D. developing SICM as a multifunctional tool for biological imaging, including developing SICM as a tool for surface charge mapping as well as FEM models for SICM studies. Currently he is working in further developing the SICM based 'lab-on-a-tip' methodology.

Viacheslav Shkirskiy is a Marie Skłodowska-Curie Research Fellow in the Department of Chemistry at the University of Warwick (UK). He obtained his Ph.D. degree in physical and analytical chemistry from the University of Pierre and Marie Curie in Paris (France) in 2015. After brief postdocs there and at Max Plank Institute for Iron Research in Düsseldorf (Germany) supported by DAAD, he joined the group of Prof. Pat Unwin in 2018 supported by a grant from European Commission (H2020-MSCA-IF). His current research is focused on the development of nanoscale SEPMs for probing light alloy reactivity.

Patrick Unwin earned his B.Sc. (Liverpool), D.Phil. (Oxford) and D.Sc. (Warwick). He is Professor of Chemistry and Director of the Centre for Doctoral Training in Molecular Analytical Science at the University of Warwick. Pat and his group are particularly well known for pioneering innovative nanoscale electrochemical imaging techniques of wide applicability. Pat is the author of more than 350 papers and book chapters, and has won a number of awards, most recently the 2018 Charles N. Reilley Award of the Society of Electroanalytical Chemistry and the 2017 International Society of Electrochemistry - Elsevier Prize for Experimental Electrochemistry.

Author Information

Corresponding Author

*P.R.Unwin@warwick.ac.uk (P.R.U.)

Notes

The authors declare no competing financial interest.

Acknowledgements

C.L.B. acknowledges financial support from the Ramsay Memorial Fellowship Trust. J.E. thanks EPSRC for a Ph.D. studentship through the EPSRC Centre for Doctoral Training in

Molecular Analytical Science, grant number EP/L015307/1. G.N.M. acknowledges financial support from the European Union's Horizon 2020 research and innovation programme under the Marie Skłodowska-Curie grant agreement No. 790615 (FUNNANO). D.P. was supported by a Leverhulme Trust Research Project Grant. V. S. acknowledges financial support from the European Union's Horizon 2020 research and innovation programme under grant agreement No. 792948 (NELMA). P.R.U. gratefully acknowledges support from a Royal Society Wolfson Research Merit Award.

References:

(1) Takahashi, Y.; Kumatani, A.; Shiku, H.; Matsue, T. *Anal. Chem.* **2017**, *89*, 342-357.

(2) Kang, M.; Momotenko, D.; Page, A.; Perry, D.; Unwin, P. R. *Langmuir* **2016**, *32*, 7993-8008.

(3) Nichols, R. J.; Higgins, S. J. *Acc. Chem. Res.* **2016**, *49*, 2640-2648.

(4) Nazmutdinov, R. R.; Zinkicheva, T. T.; Shermukhamedov, S. A.; Zhang, J.; Ulstrup, J. *Curr. Opin. Electrochem.* **2018**, *7*, 179-187.

(5) Bentley, C. L.; Kang, M.; Unwin, P. R. *Curr. Opin. Electrochem.* **2017**, *6*, 23-30.

(6) Page, A.; Perry, D.; Unwin, P. R. *Proc. R. Soc. A* **2017**, *473*, 20160889.

(7) Willets, K. A.; Wilson, A. J.; Sundaresan, V.; Joshi, P. B. *Chem. Rev.* **2017**, *117*, 7538-7582.

(8) Fang, Y.; Wang, H.; Yu, H.; Liu, X.; Wang, W.; Chen, H.-Y.; Tao, N. J. *Acc. Chem. Res.* **2016**, *49*, 2614-2624.

(9) Ying, Y.-L.; Ding, Z.; Zhan, D.; Long, Y.-T. *Chem. Sci.* **2017**, *8*, 3338-3348.

(10) Zhang, S.; Li, M.; Su, B.; Shao, Y. *Annual Review of Analytical Chemistry* **2018**, *11*, 265-286.

(11) Jantz, D. T.; Leonard, K. C. *Ind. Eng. Chem. Res.* **2018**, *57*, 7431-7440.

(12) Liang, Y.; Pfisterer, J. H. K.; McLaughlin, D.; Csoklich, C.; Seidl, L.; Bandarenka, A. S.; Schneider, O. *Small Methods* **2018**, *0*, 1800387.

(13) Ohtsuka, T.; Nishikata, A.; Sakairi, M.; Fushimi, K. In *Electrochemistry for Corrosion Fundamentals*, Ohtsuka, T.; Nishikata, A.; Sakairi, M.; Fushimi, K., Eds.; Springer Singapore: Singapore, 2018, pp 97-116.

(14) Barton, Z. J.; Rodríguez-López, J. *Anal. Bioanal. Chem.* **2016**, *408*, 2707-2715.

(15) Hernández-Burgos, K.; Barton, Z. J.; Rodríguez-López, J. *Chem. Mater.* **2017**, *29*, 8918-8931.

(16) Polcari, D.; Dauphin-Ducharme, P.; Mauzeroll, J. *Chem. Rev.* **2016**, *116*, 13234-13278.

(17) Lazenby, R.; White, R. *Chemosensors* **2018**, *6*, 24.

(18) Conzuelo, F.; Schulte, A.; Schuhmann, W. *Proc. R. Soc. A* **2018**, *474*, 20180409.

(19) Lin, T.-E.; Rapino, S.; Girault, H. H.; Lesch, A. *Chem. Sci.* **2018**, *9*, 4546-4554.

(20) Filice, F. P.; Ding, Z. *Analyst* **2018**, *Advance Article*, DOI: 10.1039/C1038AN01490F.

(21) Neves, M.; Martín-Yerga, D. *Biosensors* **2018**, *8*, 100.

(22) Zhang, J.; Zhou, J.; Pan, R.; Jiang, D.; Burgess, J. D.; Chen, H.-Y. *ACS Sensors* **2018**, *3*, 242-250.

(23) *Single Entity Electrochemistry*; Royal Society of Chemistry: Cambridge, UK, 2016; Vol. 193, p 558.

(24) *Electrochemistry at Nano-interfaces*; Royal Society of Chemistry: Cambridge, UK, 2018; Vol. 210, p 450.

(25) Baker, L. A. *J. Am. Chem. Soc.* **2018**, *Just Accepted Manuscript*, DOI: 10.1021/jacs.1028b09747.

(26) Bard, A. J.; Fan, F. R. F.; Kwak, J.; Lev, O. *Anal. Chem.* **1989**, *61*, 132-138.

(27) Engstrom, R. C.; Weber, M.; Wunder, D. J.; Burgess, R.; Winquist, S. *Anal. Chem.* **1986**, *58*, 844-848.

(28) Zoski, C. G. *J. Electrochem. Soc.* **2016**, *163*, H3088-H3100.

(29) Huang, L.; Li, Z.; Lou, Y.; Cao, F.; Zhang, D.; Li, X. *Materials* **2018**, *11*, 1389-1389.

(30) Izquierdo, J.; Knittel, P.; Kranz, C. *Anal. Bioanal. Chem.* **2018**, *410*, 307-324.

(31) Kwak, J.; Bard, A. J. *Anal. Chem.* **1989**, *61*, 1221-1227.

(32) Bard, A. J.; Mirkin, M. V.; Unwin, P. R.; Wipf, D. O. *J. Phys. Chem.* **1992**, *96*, 1861-1868.

(33) Bae, J. H.; Yu, Y.; Mirkin, M. V. *J. Phys. Chem. Lett.* **2017**, *8*, 1338-1342.

(34) Kai, T.; Zhou, M.; Duan, Z.; Henkelman, G. A.; Bard, A. J. *J. Am. Chem. Soc.* **2017**, *139*, 18552-18557.

(35) Kai, T.; Zhou, M.; Johnson, S.; Ahn, H. S.; Bard, A. J. *J. Am. Chem. Soc.* **2018**.

(36) Xiong, J.; Chen, Q.; Edwards, M. A.; White, H. S. *ACS Nano* **2015**, *9*, 8520-8529.

(37) Chen, Q.; McKelvey, K.; Edwards, M. A.; White, H. S. *J. Phys. Chem. C* **2016**, *120*, 17251-17260.

(38) Tan, S.-y.; Perry, D.; Unwin, P. R. *J. Electroanal. Chem.* **2018**, *819*, 240-250.

(39) Meloni, G. N. *Anal. Chem.* **2017**, *89*, 8643-8649.

(40) Kim, J.; Renault, C.; Nioradze, N.; Arroyo-Curras, N.; Leonard, K. C.; Bard, A. J. *Anal. Chem.* **2016**, *88*, 10284–10289.

(41) Amemiya, S.; Bard, A. J.; Fan, F.-R. F.; Mirkin, M. V.; Unwin, P. R. *Annual Review of Analytical Chemistry* **2008**, *1*, 95-131.

(42) Mirkin, M. V.; Sun, T.; Yu, Y.; Zhou, M. *Acc. Chem. Res.* **2016**, *49*, 2328-2335.

(43) O'Neil, G. D.; Kuo, H.-w.; Lomax, D. N.; Wright, J.; Esposito, D. V. *Anal. Chem.* **2018**, *90*, 11531-11537.

(44) Kai, T.; Zoski, C. G.; Bard, A. J. *Chem. Commun.* **2018**, *54*, 1934-1947.

(45) Wang, Y.; Shan, X.; Tao, N. *Faraday Discuss.* **2016**, *193*, 9-39.

(46) Edwards, M. A.; Robinson, D. A.; Ren, H.; Cheyne, C. G.; Tan, C. S.; White, H. S. *Faraday Discuss.* **2018**, *210*, 9-28.

(47) Patel, A. N.; Kranz, C. *Annual Review of Analytical Chemistry* **2018**, *11*, 329-350.

(48) Kim, J.; Shen, M.; Nioradze, N.; Amemiya, S. *Anal. Chem.* **2012**, *84*, 3489-3492.

(49) Jedraszko, J.; Michalak, M.; Jönsson-Niedziolka, M.; Nogala, W. *J. Electroanal. Chem.* **2018**, *815*, 231-237.

(50) Gossage, Z. T.; Simpson, B. H.; Schorr, N. B.; Rodríguez-López, J. *Anal. Chem.* **2016**, *88*, 9897-9901.

(51) Welle, Theresa M.; Alanis, K.; Colombo, M. L.; Sweedler, J. V.; Shen, M. *Chem. Sci.* **2018**, *9*, 4937-4941.

(52) Paixão, T. R. L. C.; Bertotti, M. *Quim. Nova* **2009**, *32*, 1306-1314.

(53) Clausmeyer, J.; Schuhmann, W. *TrAC, Trends Anal. Chem.* **2016**, *79*, 46-59.

(54) Zoski, C. G. *Electroanalysis* **2002**, *14*, 1041-1051.

(55) Yu, Y.; Noël, J.-M.; Mirkin, M. V.; Gao, Y.; Mashtalir, O.; Friedman, G.; Gogotsi, Y. *Anal. Chem.* **2014**, *86*, 3365-3372.

(56) Sun, P.; Mirkin, M. V. *Anal. Chem.* **2007**, *79*, 5809-5816.

(57) Wilde, P.; Quast, T.; Aiyappa, H. B.; Chen, Y.-T.; Botz, A.; Tarnev, T.; Marquitan, M.; Feldhege, S.; Lindner, A.; Andronescu, C.; Schuhmann, W. *ChemElectroChem* **2018**, *5*, 3083-3088.

(58) Perry, D.; Momotenko, D.; Lazenby, R. A.; Kang, M.; Unwin, P. R. *Anal. Chem.* **2016**, *88*, 5523-5530.

(59) Meloni, G. N.; Bertotti, M. *PLoS One* **2017**, *12*, e0182000.

(60) Stephens, L. I.; Mauzeroll, J. *Anal. Chem.* **2018**, *90*, 6796-6803.

(61) Filice, F. P.; Li, M. S. M.; Ding, Z. *Advanced Theory and Simulations* **2018**, 1800124.

(62) Nogala, W.; Velmurugan, J.; Mirkin, M. V. *Anal. Chem.* **2012**, *84*, 5192-5197.

(63) Kim, J.; Renault, C.; Nioradze, N.; Arroyo-Currás, N.; Leonard, K. C.; Bard, A. J. *J. Am. Chem. Soc.* **2016**, *138*, 8560-8568.

(64) Thakar, R.; Weber, A. E.; Morris, C. A.; Baker, L. A. *Analyst* **2013**, *138*, 5973-5982.

(65) Chen, R.; Hu, K.; Yu, Y.; Mirkin, M. V.; Amemiya, S. *J. Electrochem. Soc.* **2016**, *163*, H3032-H3037.

(66) Lazenby, R. A.; McKelvey, K.; Peruffo, M.; Baghdadi, M.; Unwin, P. R. *J. Solid State Electrochem.* **2013**, *17*, 2979-2987.

(67) Lazenby, R. A.; McKelvey, K.; Unwin, P. R. *Anal. Chem.* **2013**, *85*, 2937-2944.

(68) Abad, J. M.; Tesio, A. Y.; Martínez-Periñán, E.; Pariente, F.; Lorenzo, E. *J. Nano Research* **2018**, *11*, 4232-4244.

(69) Nioradze, N.; Chen, R.; Kim, J.; Shen, M.; Santhosh, P.; Amemiya, S. *Anal. Chem.* **2013**, *85*, 6198-6202.

(70) Takahashi, Y.; Shevchuk, A. I.; Novak, P.; Zhang, Y.; Ebejer, N.; Macpherson, J. V.; Unwin, P. R.; Pollard, A. J.; Roy, D.; Clifford, C. A.; Shiku, H.; Matsue, T.; Klenerman, D.; Korchev, Y. E. *Angew. Chem. Int. Ed.* **2011**, *50*, 9638-9642.

(71) Nadappuram, B. P.; McKelvey, K.; Byers, J. C.; Güell, A. G.; Colburn, A. W.; Lazenby, R. A.; Unwin, P. R. *Anal. Chem.* **2015**, *87*, 3566-3573.

(72) Gao, R.; Ying, Y. L.; Li, Y. J.; Hu, Y. X.; Yu, R. J.; Lin, Y.; Long, Y. T. *Angew. Chem., Int. Ed.* **2018**, *57*, 1011-1015.

(73) Gao, R.; Ying, Y. L.; Hu, Y. X.; Li, Y. J.; Long, Y. T. *Anal. Chem.* **2017**, *89*, 7382-7387.

(74) Wang, F.-F.; Wang, W.; He, X.; Han, L.; Zhou, J.-Z.; Tian, Z.-Q.; Tian, Z.-W.; Zhan, D. *Science China Chemistry* **2017**, *60*, 649-655.

(75) Ying, Y. L.; Hu, Y. X.; Gao, R.; Yu, R. J.; Gu, Z.; Lee, L. P.; Long, Y. T. *J. Am. Chem. Soc.* **2018**, *140*, 5385-5392.

(76) Hao, R.; Fan, Y.; Zhang, B. *J. Am. Chem. Soc.* **2017**, *139*, 12274-12282.

(77) Hao, R.; Fan, Y.; Han, C.; Zhang, B. *Anal. Chem.* **2017**, *89*, 12652-12658.

(78) Ye, Z.; Zhu, Z.; Zhang, Q.; Liu, X.; Zhang, J.; Cao, F. *Corros. Sci.* **2018**, *143*, 221-228.

(79) Chen, X.; Botz, A. J. R.; Masa, J.; Schuhmann, W. *J. Solid State Electrochem.* **2016**, *20*, 1019-1027.

(80) Ritzert, N. L.; Szalai, V. A.; Moffat, T. P. *Langmuir* **2018**, *Article ASAP*, DOI: 10.1021/acs.langmuir.1028b02731.

(81) Hui, J.; Burgess, M.; Zhang, J.; Rodríguez-López, J. *ACS Nano* **2016**, *10*, 4248-4257.

(82) Gossage, Z. T.; Schorr, N. B.; Hernández-Burgos, K.; Hui, J.; Simpson, B. H.; Montoto, E. C.; Rodríguez-López, J. *Langmuir* **2017**, *33*, 9455-9463.

(83) Blanchard, P. Y.; Sun, T.; Yu, Y.; Wei, Z.; Matsui, H.; Mirkin, M. V. *Langmuir* **2016**, *32*, 2500-2508.

(84) Yu, Y.; Sun, T.; Mirkin, M. V. *Anal. Chem.* **2015**, *87*, 7446-7453.

(85) O'Connell, M. A.; Wain, A. J. *Anal. Methods* **2015**, *7*, 6983-6999.

(86) Takahashi, Y.; Shevchuk, A. I.; Novak, P.; Babakinejad, B.; Macpherson, J.; Unwin, P. R.; Shiku, H.; Gorelik, J.; Klenerman, D.; Korchev, Y. E.; Matsue, T. *Proc. Natl. Acad. Sci. U. S. A.* **2012**, *109*, 11540-11545.

(87) Sundaresan, V.; Marchuk, K.; Yu, Y.; Titus, E. J.; Wilson, A. J.; Armstrong, C. M.; Zhang, B.; Willets, K. A. *Anal. Chem.* **2017**, *89*, 922-928.

(88) Chen, C.-C.; Zhou, Y.; Baker, L. A. *Annual Review of Analytical Chemistry* **2012**, *5*, 207-228.

(89) Hansma, P. K.; Drake, B.; Marti, O.; Gould, S.; Prater, C. *Science* **1989**, *243*, 641-643.

(90) Korchev, Y. E.; Bashford, C. L.; Milovanovic, M.; Vodyanoy, I.; Lab, M. J. *Biophys. J.* **1997**, *73*, 653-658.

(91) Shevchuk, A. I.; Frolenkov, G. I.; Sánchez, D.; James, P. S.; Freedman, N.; Lab, M. J.; Jones, R.; Klenerman, D.; Korchev, Y. E. *Angew. Chem.* **2006**, *118*, 2270-2274.

(92) Korchev, Y. E.; Gorelik, J.; Lab, M. J.; Sviderskaya, E. V.; Johnston, C. L.; Coombes, C. R.; Vodyanoy, I.; Edwards, C. R. *Biophys. J.* **2000**, *78*, 451-457.

(93) Takahashi, Y.; Murakami, Y.; Nagamine, K.; Shiku, H.; Aoyagi, S.; Yasukawa, T.; Kanzaki, M.; Matsue, T. *Phys. Chem. Chem. Phys.* **2010**, *12*, 10012-10017.

(94) Novak, P.; Li, C.; Shevchuk, A. I.; Stepanyan, R.; Caldwell, M.; Hughes, S.; Smart, T. G.; Gorelik, J.; Ostanin, V. P.; Lab, M. J. *Nat. Methods* **2009**, *6*, 279.

(95) McKelvey, K.; Perry, D.; Byers, J. C.; Colburn, A. W.; Unwin, P. R. *Anal. Chem.* **2014**, *86*, 3639-3646.

(96) Shevchuk, A. I.; Gorelik, J.; Harding, S. E.; Lab, M. J.; Klenerman, D.; Korchev, Y. E. *Biophys. J.* **2001**, *81*, 1759-1764.

(97) Rheinlaender, J.; Geisse, N. A.; Proksch, R.; Schäffer, T. E. *Langmuir* **2010**, *27*, 697-704.

(98) McKelvey, K.; Kinnear, S. L.; Perry, D.; Momotenko, D.; Unwin, P. R. *J. Am. Chem. Soc.* **2014**, *136*, 13735-13744.

(99) Perry, D.; Al Botros, R.; Momotenko, D.; Kinnear, S. L.; Unwin, P. R. *ACS Nano* **2015**, *9*, 7266-7276.

(100) Sa, N.; Lan, W.-J.; Shi, W.; Baker, L. A. *ACS Nano* **2013**, *7*, 11272-11282.

(101) Perry, D.; Paulose Nadappuram, B.; Momotenko, D.; Voyias, P. D.; Page, A.; Tripathi, G.; Frenguelli, B. G.; Unwin, P. R. *J. Am. Chem. Soc.* **2016**, *138*, 3152-3160.

(102) Zhu, C.; Zhou, L.; Choi, M.; Baker, L. A. *ChemElectroChem* **2018**, *5*, 2986-2990.

(103) Zhu, C.; Shi, W.; Daleke, D. L.; Baker, L. A. *Analyst* **2018**, *143*, 1087-1093.

(104) Ida, H.; Takahashi, Y.; Kumatani, A.; Shiku, H.; Matsue, T. *Anal. Chem.* **2017**, *89*, 6015-6020.

(105) Seifert, J.; Rheinlaender, J.; Lang, F.; Gawaz, M.; Schäffer, T. E. *Sci. Rep.* **2017**, *7*, 4810.

(106) Seifert, J.; Rheinlaender, J.; Schäffer, T. E. *Jpn. J. Appl. Phys.* **2018**, *57*, 08NB02.

(107) Hagemann, P.; Gesper, A.; Happel, P. *ACS Nano* **2018**, *12*, 5807–5815.

(108) Lee, K.-D.; Hong, K.; Papahadjopoulos, D. *Biochim. Biophys. Acta* **1992**, *1103*, 185-197.

(109) Chung, T.-H.; Wu, S.-H.; Yao, M.; Lu, C.-W.; Lin, Y.-S.; Hung, Y.; Mou, C.-Y.; Chen, Y.-C.; Huang, D.-M. *Biomaterials* **2007**, *28*, 2959-2966.

(110) Stratmann, M.; Frankel, G. S. In *Corrosion and Oxide Films*, Bard, A. J.; Stratmann, M., Eds.; Wiley-VCH, 2001.

(111) Muster, T. H.; Cole, I. S. *Corros. Sci.* **2004**, *46*, 2319-2335.

(112) McCafferty, E. *J. Electrochem. Soc.* **1999**, *146*, 2863-2863.

(113) Page, A.; Perry, D.; Young, P.; Mitchell, D.; Frenguelli, B. G.; Unwin, P. R. *Anal. Chem.* **2016**, *88*, 10854-10859.

(114) Klausen, L. H.; Fuhs, T.; Dong, M. *Nat. Comm.* **2016**, *7*, 12447.

(115) Clarke, R. W.; Zhukov, A.; Richards, O.; Johnson, N.; Ostanin, V.; Klenerman, D. *J. Am. Chem. Soc.* **2012**, *135*, 322-329.

(116) Perry, D.; Page, A.; Chen, B.; Frenguelli, B. G.; Unwin, P. R. *Anal. Chem.* **2017**, *89*, 12458-12465.

(117) Tognoni, E.; Baschieri, P.; Ascoli, C.; Pellegrini, M.; Pellegrino, M. *Micron* **2016**, *83*, 11-18.

(118) Momotenko, D.; McKelvey, K.; Kang, M.; Meloni, G. N.; Unwin, P. R. *Anal. Chem.* **2016**, *88*, 2838-2846.

(119) Kang, M.; Perry, D.; Bentley, C. L.; West, G.; Page, A.; Unwin, P. R. *ACS Nano* **2017**, *11*, 9525-9535.

(120) Choi, M.; Baker, L. A. *Anal. Chem.* **2018**, *90*, 11797-11801.

(121) Patel, A. N.; McKelvey, K.; Unwin, P. R. *J. Am. Chem. Soc.* **2012**, *134*, 20246-20249.

(122) Shi, W.; Zeng, Y.; Zhou, L.; Xiao, Y.; Cummins, T. R.; Baker, L. A. *Faraday Discuss.* **2016**, *193*, 81-97.

(123) Macazo, F. C.; White, R. J. *J. Am. Chem. Soc.* **2016**, *138*, 2793-2801.

(124) Nascimento, R. A.; Özel, R. E.; Mak, W. H.; Mulato, M.; Singaram, B.; Pourmand, N. *Nano Lett.* **2016**, *16*, 1194-1200.

(125) Chen, C.-C.; Zhou, Y.; Morris, C. A.; Hou, J.; Baker, L. A. *Anal. Chem.* **2013**, *85*, 3621-3628.

(126) Zhou, Y.; Chen, C. C.; Weber, A. E.; Zhou, L.; Baker, L. A.; Hou, J. *Tissue Barriers* **2013**, *1*, e25585.

(127) Zhou, L.; Gong, Y.; Hou, J.; Baker, L. A. *Anal. Chem.* **2017**, *89*, 13603-13609.

(128) Zhou, L.; Gong, Y.; Sunq, A.; Hou, J.; Baker, L. A. *Anal. Chem.* **2016**, *88*, 9630-9637.

(129) Shevchuk, A.; Tokar, S.; Gopal, S.; Sanchez-Alonso, J. L.; Tarasov, A. I.; Vélez-Ortega, A. C.; Chiappini, C.; Rorsman, P.; Stevens, M. M.; Gorelik, J. *Biophys. J.* **2016**, *110*, 2252-2265.

(130) Zhuang, J.; Jiao, Y.; Mugabo, V. *Micron* **2017**, *101*, 177-185.

(131) Zhuang, J.; Guo, R.; Li, F.; Yu, D. *Meas. Sci. Technol.* **2016**, *27*, 085402.

(132) Gesper, A.; Hagemann, P.; Happel, P. *Nanoscale* **2017**, *9*, 14172-14183.

(133) Schierbaum, N.; Hack, M.; Betz, O.; Schäffer, T. E. *Anal. Chem.* **2018**, *90*, 5048-5054.

(134) Watanabe, S.; Ando, T. *Appl. Phys. Lett.* **2017**, *111*, 113106.

(135) Rheinlaender, J.; Schäffer, T. E. *Anal. Chem.* **2017**, *89*, 11875-11880.

(136) Binnig, G.; Rohrer, H.; Gerber, C.; Weibel, E. *Phys. Rev. Lett.* **1982**, *49*, 57-61.

(137) Elliott, M. *Curr. Opin. Electrochem.* **2017**, *4*, 152-158.

(138) Hodnik, N.; Dehm, G.; Mayrhofer, K. J. J. *Acc. Chem. Res.* **2016**, *49*, 2015-2022.

(139) Bussetti, G.; Yivlialin, R.; Alliata, D.; Li Bassi, A.; Castiglioni, C.; Tommasini, M.; Casari, C. S.; Passoni, M.; Biagioni, P.; Ciccacci, F.; Duò, L. *J. Phys. Chem. C* **2016**, *120*, 6088-6093.

(140) Bui, N. N.; Ledina, M.; Reber, T. J.; Jung, J.; Stickney, J. L. *ACS Nano* **2017**, *11*, 9481-9489.

(141) Gu, J.-Y.; Cai, Z.-F.; Wang, D.; Wan, L.-J. *ACS Nano* **2016**, *10*, 8746-8750.

(142) Jacobse, L.; Huang, Y.-F.; Koper, M. T. M.; Rost, M. J. *Nat. Mater.* **2018**, *17*, 277-282.

(143) Deng, X.; Galli, F.; Koper, M. T. M. *J. Am. Chem. Soc.* **2018**, *140*, 13285-13291.

(144) Schnaidt, J.; Beckord, S.; Engstfeld, A. K.; Klein, J.; Brimaud, S.; Behm, R. J. *Phys. Chem. Chem. Phys.* **2017**, *19*, 4166-4178.

(145) Wen, R.; Rahn, B.; Magnussen, O. M. *J. Phys. Chem. C* **2016**, *120*, 15765-15771.

(146) Matsushima, H.; Lin, S. W.; Morin, S.; Magnussen, O. M. *Faraday Discuss.* **2016**, *193*, 171-185.

(147) Pfisterer, J. H. K.; Liang, Y.; Schneider, O.; Bandarenka, A. S. *Nature* **2017**, *549*, 74.

(148) Page, A.; Kang, M.; Armitstead, A.; Perry, D.; Unwin, P. R. *Anal. Chem.* **2017**, *89*, 3021-3028.

(149) Takahashi, Y.; Ida, H.; Matsumae, Y.; Komaki, H.; Zhou, Y.; Kumatani, A.; Kanzaki, M.; Shiku, H.; Matsue, T. *Phys. Chem. Chem. Phys.* **2017**, *19*, 26728-26733.

(150) Macpherson, J. V.; Unwin, P. R. *Anal. Chem.* **2000**, *72*, 276-285.

(151) Kranz, C.; Friedbacher, G.; Mizaikoff, B.; Lugstein, A.; Smoliner, J.; Bertagnolli, E. *Anal. Chem.* **2001**, *73*, 2491-2500.

(152) Knittel, P.; Mizaikoff, B.; Kranz, C. *Anal. Chem.* **2016**, *88*, 6174-6178.

(153) Huang, Z.; De Wolf, P.; Poddar, R.; Li, C.; Mark, A.; Nellist, M. R.; Chen, Y.; Jiang, J.; Papastavrou, G.; Boettcher, S. W.; Xiang, C.; Brunschwig, B. S. *Microscopy Today* **2016**, *24*, 18-25.

(154) Knittel, P.; Bibikova, O.; Kranz, C. *Faraday Discuss.* **2016**, *193*, 353-369.

(155) Guin, S. K.; Knittel, P.; Daboss, S.; Breusow, A.; Kranz, C. *Chem. Asian J.* **2017**, *12*, 1615-1624.

(156) Michael, R. N.; Yikai, C.; Andreas, M.; Sebastian, G.; Christian, S.; Jingjing, J.; Rakesh, P.; Chunzeng, L.; Ravi, K.; Georg, P.; Markus, R.; Bruce, S. B.; Zhuangqun, H.; Chengxiang, X.; Shannon, W. B. *Nanotechnology* **2017**, *28*, 095711.

(157) Zhang, G.; Cuharuc, A. S.; Güell, A. G.; Unwin, P. R. *Phys. Chem. Chem. Phys.* **2015**, *17*, 11827-11838.

(158) Unwin, P. R.; Güell, A. G.; Zhang, G. *Acc. Chem. Res.* **2016**, *49*, 2041-2048.

(159) Liu, Y.; Holzinger, A.; Knittel, P.; Poltorak, L.; Gamero-Quijano, A.; Rickard, W. D. A.; Walcarius, A.; Herzog, G.; Kranz, C.; Arrigan, D. W. M. *Anal. Chem.* **2016**, *88*, 6689-6695.

(160) Velmurugan, J.; Agrawal, A.; An, S.; Choudhary, E.; Szalai, V. A. *Anal. Chem.* **2017**, *89*, 2687-2691.

(161) Izquierdo, J.; Eifert, A.; Kranz, C.; Souto, R. M. *Electrochim. Acta* **2017**, *247*, 588-599.

(162) Anne, A.; Cambril, E.; Chovin, A.; Demaille, C. *Anal. Chem.* **2010**, *82*, 6353-6362.

(163) Chennit, K.; Trasobares, J.; Anne, A.; Cambril, E.; Chovin, A.; Clément, N.; Demaille, C. *Anal. Chem.* **2017**, *89*, 11061-11069.

(164) Tavert-Roudet, G.; Anne, A.; Barra, A.; Chovin, A.; Demaille, C.; Michon, T. *Mol. Plant. Microbe Interact.* **2017**, *30*, 754-762.

(165) Anne, A.; Chovin, A.; Demaille, C.; Michon, T. In *Virus-Derived Nanoparticles for Advanced Technologies: Methods and Protocols*, Wege, C.; Lomonossoff, G. P., Eds.; Springer New York: New York, NY, 2018, pp 455-470.

(166) Frey, C. M.; Eifert, A.; Schütz, H.; Barth, H.; Mizaikoff, B.; Kranz, C. *Electrochim. Acta* **2016**, *209*, 341-349.

(167) Knittel, P.; Zhang, H.; Kranz, C.; Wallace, G. G.; Higgins, M. J. *Nanoscale* **2016**, *8*, 4475-4481.

(168) Nellist, M. R.; Laskowski, F. A. L.; Qiu, J.; Hajibabaei, H.; Sivula, K.; Hamann, T. W.; Boettcher, S. W. *Nat. Energy* **2018**, *3*, 46-52.

(169) Deng, J.; Nellist, M. R.; Stevens, M. B.; Dette, C.; Wang, Y.; Boettcher, S. W. *Nano Lett.* **2017**, *17*, 6922-6926.

(170) Dorwling-Carter, L.; Aramesh, M.; Han, H.; Zambelli, T.; Momotenko, D. *Anal. Chem.* **2018**, *90*, 11453-11460.

(171) Ossola, D.; Dorwling-Carter, L.; Dermutz, H.; Behr, P.; Vörös, J.; Zambelli, T. *Phys. Rev. Lett.* **2015**, *115*, 238103.

(172) Dorwling-Carter, L.; Aramesh, M.; Forró, C.; Tiefenauer, R. F.; Shorubalko, I.; Vörös, J.; Zambelli, T. *J. Appl. Phys.* **2018**, *124*, 174902.

(173) Momotenko, D.; Page, A.; Adobes-Vidal, M.; Unwin, P. R. *ACS Nano* **2016**, *10*, 8871-8878.

(174) Hirt, L.; Grüter, R. R.; Berthelot, T.; Cornut, R.; Vörös, J.; Zambelli, T. *RSC Adv.* **2015**, *5*, 84517-84522.

(175) Meier, J.; Friedrich, K. A.; Stimming, U. *Faraday Discuss.* **2002**, *121*, 365-372.

(176) Treutler, T. H.; Wittstock, G. *Electrochim. Acta* **2003**, *48*, 2923-2932.

(177) Sun, T.; Wang, D.; Mirkin, M. V. *Angew. Chem. Int. Ed.* **2018**, *57*, 7463-7467.

(178) Sun, T.; Wang, D.; Mirkin, Michael V. *Faraday Discuss.* **2018**, *210*, 173-188.

(179) Ebejer, N.; Güell, A. G.; Lai, S. C. S.; McKelvey, K.; Snowden, M. E.; Unwin, P. R. In *Annual Review of Analytical Chemistry, Vol 6*, Cooks, R. G.; Pemberton, J. E., Eds.; Annual Reviews: Palo Alto, 2013, pp 329-351.

(180) Aaronson, B. D. B.; Guell, A. G.; McKelvey, K.; Momotenko, D.; Unwin, P. R. In *Nanoelectrochemistry*; CRC Press, 2015, pp 655-694.

(181) Bentley, C. L.; Perry, D.; Unwin, P. R. *Anal. Chem.* **2018**, *90*, 7700-7707.

(182) Bentley, C. L.; Kang, M.; Unwin, P. R. *J. Am. Chem. Soc.* **2017**, *139*, 16813-16821.

(183) E, S. P.; Kim, Y.-R.; Perry, D.; Bentley, C. L.; Unwin, P. R. *ACS Appl. Mater. Interfaces* **2016**, *8*, 30458–30466.

(184) Mariano, R. G.; McKelvey, K.; White, H. S.; Kanan, M. W. *Science* **2017**, *358*, 1187-1192.

(185) Bentley, C. L.; Andronescu, C.; Smialkowski, M.; Kang, M.; Tarnev, T.; Marler, B.; Unwin, P. R.; Apfel, U. P.; Schuhmann, W. *Angew. Chem. Int. Ed.* **2018**, *57*, 4093-4097.

(186) Suter, T.; Böhni, H. *Electrochim. Acta* **1997**, *42*, 3275-3280.

(187) Andreatta, F.; Fedrizzi, L. *Electrochim. Acta* **2016**, *203*, 337-349.

(188) Williams, C. G.; Edwards, M. A.; Colley, A. L.; Macpherson, J. V.; Unwin, P. R. *Anal. Chem.* **2009**, *81*, 2486-2495.

(189) Takahashi, Y.; Kumatani, A.; Munakata, H.; Inomata, H.; Ito, K.; Ino, K.; Shiku, H.; Unwin, P. R.; Korchev, Y. E.; Kanamura, K.; Matsue, T. *Nat. Comm.* **2014**, *5*, 1-7.

(190) Bentley, C. L.; Unwin, P. R. *Faraday Discuss.* **2018**, *210*, 365-379.

(191) Snowden, M. E.; Güell, A. G.; Lai, S. C. S.; McKelvey, K.; Ebejer, N.; O'Connell, M. A.; Colburn, A. W.; Unwin, P. R. *Anal. Chem.* **2012**, *84*, 2483-2491.

(192) Alzahrani, H.; Bentley, C.; Burrows, R.; Cao, C.; Cai, Q.; Chikere, C.; Crooks, R. M.; Dunevall, J.; Edwards, M.; Ewing, A.; Gao, R.; Hillman, R.; Kahram, M.; Kanoufi, F.; Kranz, C.; Lemineur, J.-F.; Long, Y.; McKelvey, K.; Mirkin, M.; Moore, S.; Nogala, W.; Ren, H.; Schuhmann, W.; Unwin, P.; Vezzoli, A.; White, H.; Willets, K.; Yang, Z.; Ying, Y. *Faraday Discuss.* **2018**, *210*, 451-479.

(193) Bentley, C. L.; Kang, M.; Maddar, F. M.; Li, F.; Walker, M.; Zhang, J.; Unwin, P. R. *Chem. Sci.* **2017**, *8*, 6583-6593.

(194) Patel, A. N.; Collignon, M. G.; O'Connell, M. A.; Hung, W. O. Y.; McKelvey, K.; Macpherson, J. V.; Unwin, P. R. *J. Am. Chem. Soc.* **2012**, *134*, 20117-20130.

(195) Güell, A. G.; Cuharuc, A. S.; Kim, Y.-R.; Zhang, G.; Tan, S.-y.; Ebejer, N.; Unwin, P. R. *ACS Nano* **2015**, *9*, 3558-3571.

(196) Ustarroz, J.; Ornelas, I. M.; Zhang, G.; Perry, D.; Kang, M.; Bentley, C. L.; Walker, M.; Unwin, P. R. *ACS Catal.* **2018**, *8*, 6775-6790.

(197) Chen, C.-H.; Meadows, K. E.; Cuharuc, A.; Lai, S. C. S.; Unwin, P. R. *Phys. Chem. Chem. Phys.* **2014**, *16*, 18545-18552.

(198) Snowden, M. E.; Dayeh, M.; Payne, N. A.; Gervais, S.; Mauzeroll, J.; Schougaard, S. B. *J. Power Sources* **2016**, *325*, 682-689.

(199) E, S. P.; Kang, M.; Wilson, P.; Meng, L.; Perry, D.; Basile, A.; Unwin, P. R. *Chem. Commun.* **2018**, *54*, 3053-3056.

(200) Ebejer, N.; Schnippering, M.; Colburn, A. W.; Edwards, M. A.; Unwin, P. R. *Anal. Chem.* **2010**, *82*, 9141-9145.

(201) Kinnear, S. L.; McKelvey, K.; Snowden, M. E.; Peruffo, M.; Colburn, A. W.; Unwin, P. R. *Langmuir* **2013**, *29*, 15565-15572.

(202) Parker, A. S.; Al Botros, R.; Kinnear, S. L.; Snowden, M. E.; McKelvey, K.; Ashcroft, A. T.; Carvell, M.; Joiner, A.; Peruffo, M.; Philpotts, C.; Unwin, P. R. *J. Colloid Interface Sci.* **2016**, *476*, 94-102.

(203) Güell, A. G.; Meadows, K. E.; Dudin, P. V.; Ebejer, N.; Macpherson, J. V.; Unwin, P. R. *Nano Lett.* **2014**, *14*, 220-224.

(204) McKelvey, K.; O'Connell, M. A.; Unwin, P. R. *Chem. Commun.* **2013**, *49*, 2986-2988.

(205) Patten, H. V.; Hutton, L. A.; Webb, J. R.; Newton, M. E.; Unwin, P. R.; Macpherson, J. V. *Chem. Commun.* **2015**, *51*, 164-167.

(206) Momotenko, D.; Byers, J. C.; McKelvey, K.; Kang, M.; Unwin, P. R. *ACS Nano* **2015**, *9*, 8942-8952.

(207) Chen, C.-H.; Jacobse, L.; McKelvey, K.; Lai, S. C. S.; Koper, M. T. M.; Unwin, P. R. *Anal. Chem.* **2015**, *87*, 5782-5789.

(208) Li, Q.; Xie, S.; Liang, Z.; Meng, X.; Liu, S.; Girault, H. H.; Shao, Y. *Angew. Chem. Int. Ed.* **2009**, *48*, 8010-8013.

(209) Salançon, E.; Tinland, B. *Beilstein J. Nanotechnol.* **2018**, *9*, 2181-2187.

(210) Byers, J. C.; Güell, A. G.; Unwin, P. R. *J. Am. Chem. Soc.* **2014**, *136*, 11252-11255.

(211) Cobb, S. J.; Ayres, Z. J.; Macpherson, J. V. *Annual Review of Analytical Chemistry* **2018**, *11*, 463-484.

(212) Maddar, F. M.; Lazenby, R. A.; Patel, A. N.; Unwin, P. R. *Phys. Chem. Chem. Phys.* **2016**, *18*, 26404-26411.

(213) Aaronson, B. D. B.; Chen, C. H.; Li, H. J.; Koper, M. T. M.; Lai, S. C. S.; Unwin, P. R. *J. Am. Chem. Soc.* **2013**, *135*, 3873-3880.

(214) Liu, D.-Q.; Chen, C.-H.; Perry, D.; West, G.; Cobb, S. J.; Macpherson, J. V.; Unwin, P. R. *ChemElectroChem* **2018**, *5*, DOI: 10.1002/celc.201800770.

(215) Seh, Z. W.; Kibsgaard, J.; Dickens, C. F.; Chorkendorff, I.; Nørskov, J. K.; Jaramillo, T. F. *Science* **2017**, *355*, 146.

(216) Benck, J. D.; Hellstern, T. R.; Kibsgaard, J.; Chakthranont, P.; Jaramillo, T. F. *ACS Catal.* **2014**, *4*, 3957-3971.

(217) Jaramillo, T. F.; Jørgensen, K. P.; Bonde, J.; Nielsen, J. H.; Horch, S.; Chorkendorff, I. *Science* **2007**, *317*, 100-102.

(218) E, S. P.; Liu, D.; Lazenby, R. A.; Sloan, J.; Vidotti, M.; Unwin, P. R.; Macpherson, J. V. *J. Phys. Chem. C* **2016**, *120*, 16059-16068.

(219) Zhang, G.; Güell, A. G.; Kirkman, P. M.; Lazenby, R. A.; Miller, T. S.; Unwin, P. R. *ACS Appl. Mater. Interfaces* **2016**, *8*, 8008-8016.

(220) Saha, P.; Hill, J. W.; Walmsley, J. D.; Hill, C. M. *Anal. Chem.* **2018**, *Just accepted manuscript*, DOI: 10.1021/acs.analchem.1028b03360.

(221) Dayeh, M.; Ghavidel, M. R. Z.; Mauzeroll, J.; Schougaard, S. B. *ChemElectroChem* **2018**, *5*, DOI: 10.1002/celc.201800750.

(222) Oseland, E. E.; Ayres, Z. J.; Basile, A.; Haddleton, D. M.; Wilson, P.; Unwin, P. R. *Chem. Commun.* **2016**, *52*, 9929-9932.

(223) Chang, W. S.; Jeong, H.; Kim, J. H.; Lee, S.; Wajahat, M.; Han, J. T.; Cho, S. H.; Seol, S. K. *Carbon* **2017**, *123*, 364-370.

(224) Chen, M.; Xu, Z.; Kim, J. H.; Seol, S. K.; Kim, J. T. *ACS Nano* **2018**, *12*, 4172-4177.

(225) Kim, J. T.; Pyo, J.; Seol, S. K.; Je, J. H. *ACS Macro Lett.* **2018**, 1267-1271.

(226) Arcadia, C. E.; Reyes, C. C.; Rosenstein, J. K. *ACS Nano* **2017**, *11*, 4907-4915.

(227) Chen, T.; Dong, B.; Chen, K.; Zhao, F.; Cheng, X.; Ma, C.; Lee, S.; Zhang, P.; Kang, S. H.; Ha, J. W.; Xu, W.; Fang, N. *Chem. Rev.* **2017**, *117*, 7510-7537.

(228) Dong, B.; Pei, Y.; Zhao, F.; Goh, T. W.; Qi, Z.; Xiao, C.; Chen, K.; Huang, W.; Fang, N. *Nature Catalysis* **2018**, *1*, 135-140.

(229) Zou, N.; Zhou, X.; Chen, G.; Andoy, N. M.; Jung, W.; Liu, G.; Chen, P. *Nat. Chem.* **2018**, *10*, 607-614.

(230) Lu, J.; Fan, Y.; Howard, M. D.; Vaughan, J. C.; Zhang, B. *J. Am. Chem. Soc.* **2017**, *139*, 2964-2971.

(231) Hao, R.; Fan, Y.; Howard, M. D.; Vaughan, J. C.; Zhang, B. *Proc. Natl. Acad. Sci. U. S. A.* **2018**, *115*, 5878-5883.

(232) Yu, Y.; Sundaresan, V.; Bandyopadhyay, S.; Zhang, Y.; Edwards, M. A.; McKelvey, K.; White, H. S.; Willets, K. A. *ACS Nano* **2017**, *11*, 10529-10538.

(233) Wang, Y.; Shan, X.; Wang, H.; Wang, S.; Tao, N. *J. Am. Chem. Soc.* **2017**, *139*, 1376-1379.

(234) Jiang, D.; Jiang, Y.; Li, Z.; Liu, T.; Wo, X.; Fang, Y.; Tao, N.; Wang, W.; Chen, H.-Y. *J. Am. Chem. Soc.* **2017**, *139*, 186-192.

(235) Yuan, L.; Tao, N.; Wang, W. *Annual Review of Analytical Chemistry* **2017**, *10*, 183-200.

(236) Wang, Y.; Shan, X.; Wang, S.; Tao, N.; Blanchard, P.-Y.; Hu, K.; Mirkin, M. V. *Anal. Chem.* **2016**, *88*, 1547-1552.

(237) Stratmann, M.; Streckel, H.; Feser, R. *Corros. Sci.* **1991**, *32*, 467-470.

(238) Rohwerder, M. In *Passivity of Metals and the Kelvin Probe Technique*; Elsevier, 2018, pp 414-422.

(239) Uebel, M.; Vimalanandan, A.; Laaboudi, A.; Evers, S.; Stratmann, M.; Diesing, D.; Rohwerder, M. *Langmuir* **2017**, *33*, 10807-10817.

(240) Jaffe, L.; Nuccitelli, R. *J. Cell Biol* **1974**, *63*, 614-628.

(241) Bastos, A. C.; Quevedo, M. C.; Karavai, O. V.; Ferreira, M. G. S. *J. Electrochem. Soc.* **2017**, *164*, C973-C990.

(242) Bobacka, J.; Ivaska, A.; Lewenstam, A. *Chem. Rev.* **2008**, *108*, 329-351.

(243) Lamaka, S.; Souto, R. M.; Ferreira, M. G. S. In *Microscopy: Science, Technology, Applications and Education*, Mendez-Vilas, A.; Diaz, J., Eds.; Formatex Research Center, 2010, pp 2162-2173.

(244) Eckhard, K.; Schuhmann, W. *Analyst* **2008**, *133*, 1486-1497.

(245) Huang, V. M.; Wu, S.-L.; Orazem, M. E.; Pébère, N.; Tribollet, B.; Vivier, V. *Electrochim. Acta* **2011**, *56*, 8048-8057.

For TOC Only: